The SAMI Galaxy Survey: Gas velocity dispersions in low-z star-forming galaxies and the drivers of turbulence

Mathew R. Varidel[1,2][⋆], Scott M. Croom[1,2], Geraint F. Lewis[1], Deanne B. Fisher[2,3],
Karl Glazebrook[2,3], Barbara Catinella[2,4], Luca Cortese[2,4], Mark R. Krumholz[2,5,6,7],
Joss Bland-Hawthorn[1,2], Julia J. Bryant[1,2,8], Brent Groves[2,4,5], Sarah Brough[2,9],
Christoph Federrath[5], Jon S. Lawrence[10], Nuria P. Lorente[11], Matt S. Owers[12,13],
Samuel N. Richards[14], Ángel R. López-Sánchez[8,12], Sarah M. Sweet[2,15],
Jesse van de Sande[1,2], and Sam P. Vaughan[1,2]

[1]*Sydney Institute for Astronomy (SIfA), School of Physics, A28, The University of Sydney, NSW 2006, Australia*
[2]*ARC Centre of Excellence for All Sky Astrophysics in 3 Dimensions (ASTRO 3D)*
[3]*Centre for Astrophysics and Supercomputing, Swinburne University of Technology, PO Box 218, Hawthorn, VIC 3122, Australia*
[4]*International Centre for Radio Astronomy Research, University of Western Australia, 35 Stirling Highway, Crawley WA 6009, Australia*
[5]*Research School of Astronomy and Astrophysics, Australian National University, Canberra, ACT 2611, Australia*
[6]*Universität Heidelberg, Zentrum für Astronomie, Institut für Theoretische Astrophysik, 69120 Heidelberg, Germany*
[7]*Max Planck Institute for Astronomy, Königstuhl 17, 69117 Heidelberg, Germany*
[8]*Australian Astronomical Optics, AAO-USydney, School of Physics, University of Sydney, NSW 2006, Australia*
[9]*School of Physics, University of New South Wales, NSW 2052, Australia*
[10]*Australian Astronomical Optics, Macquarie University, 105 Delhi Rd, North Ryde, NSW 2113, Australia*
[11]*Faculty of Science & Engineering, Macquarie University. 105 Delhi Rd, North Ryde, NSW 2113, Australia*
[12]*Department of Physics and Astronomy, Macquarie University, NSW 2109, Australia*
[13]*Astronomy, Astrophysics and Astrophotonics Research Centre, Macquarie University, Sydney, NSW 2109, Australia*
[14]*SOFIA Science Center, USRA, NASA Ames Research Center, Building N232, M/S 232-12, P.O. Box 1, Moffett Field, CA 94035-0001, USA*
[15]*School of Mathematics and Physics, University of Queensland, Brisbane, QLD 4072, Australia*

ABSTRACT

We infer the intrinsic ionised gas kinematics for 383 star-forming galaxies across a range of integrated star-formation rates (SFR $\in [10^{-3}, 10^2]$ M$_\odot$ yr^{-1}) at $z \lesssim 0.1$ using a consistent 3D forward-modelling technique. The total sample is a combination of galaxies from the SAMI Galaxy Survey and DYNAMO survey. For typical low-z galaxies taken from the SAMI Galaxy Survey, we find the vertical velocity dispersion ($\sigma_{v,z}$) to be positively correlated with measures of star-formation rate, stellar mass, H I gas mass, and rotational velocity. The greatest correlation is with star-formation rate surface density (Σ_{SFR}). Using the total sample, we find $\sigma_{v,z}$ increases slowly as a function of integrated star-formation rate in the range SFR $\in [10^{-3}, 1]$ M$_\odot$ yr^{-1} from 17 ± 3 km s^{-1} to 24 ± 5 km s^{-1} followed by a steeper increase up to $\sigma_{v,z} \sim 80$ km s^{-1} for SFR $\gtrsim 1$ M$_\odot$ yr^{-1}. This is consistent with recent theoretical models that suggest a $\sigma_{v,z}$ floor driven by star-formation feedback processes with an upturn in $\sigma_{v,z}$ at higher SFR driven by gravitational transport of gas through the disc.

Key words: galaxies: kinematics and dynamics, galaxies: evolution, techniques: imaging spectroscopy, methods: statistical, methods: data analysis

⋆ E-mail: mathew.varidel@sydney.edu.au

1 INTRODUCTION

Galaxies at $z > 1$ typically have velocity dispersions greater than nearby galaxies (Kassin et al. 2012; Wisnioski et al. 2015; Johnson et al. 2018; Übler et al. 2019). While observations of galaxies at $z > 1$ reveal a significant proportion of galaxies with velocity dispersions in the range $50 – 100$ km s^{-1} (e.g. Genzel et al. 2006; Law et al. 2007; Förster Schreiber et al. 2009; Law et al. 2009; Epinat et al. 2010; Jones et al. 2010; Lemoine-Busserolle et al. 2010), nearby galaxies typically have velocity dispersions of < 50 km s^{-1} (Epinat et al. 2008; Moiseev et al. 2015; Varidel et al. 2016; Yu et al. 2019). Although this has been observed, the process by which galaxies settle to lower velocity dispersions across epochs is not well understood.

Another important observation is that galaxies at all epochs exhibit velocity dispersions that are greater than expected by the thermal contribution of the gas alone. In the case of ionised gas measured using the Hα emission line, the characteristic temperature of 10^4 K corresponds to an expected velocity dispersion of ~9 km s^{-1} (Glazebrook 2013). Galaxies have velocity dispersions > 9 km s^{-1} at all epochs.

Studies suggest that turbulent motions above the thermal contribution dissipate on timescales of the order of the flow crossing time (Mac Low et al. 1998; Stone et al. 1998; Mac Low 1999). The crossing time for a galaxy with Toomre stability (Toomre 1964) of $Q \sim 1$ will be of order the dynamical time, which is typically $\mathcal{O}(100 \text{ Myr})$ (Krumholz et al. 2018). If the turbulent motions are on the scale of Giant Molecular Clouds (GMCs), it will decay on $\mathcal{O}(< 10 \text{ Myr})$. Therefore, we should rarely see galaxies with velocity dispersions greater than the thermal contribution, unless there is an ongoing driving mechanism to sustain the observed gas turbulence.

Numerous energetic sources have been proposed to contribute to the non-thermal turbulence observed in galaxies. These drivers can typically be split into star-formation feedback processes (Norman & Ferrara 1996; Mac Low & Klessen 2004; Krumholz & Matzner 2009; Murray et al. 2010), gravitational transport of gas onto (Elmegreen & Burkert 2010; Hopkins et al. 2013) or through (Krumholz & Burkert 2010) the disc, dynamical drivers such as shear and differential rotations across the disc (Federrath et al. 2016, 2017), or interactions between galaxy components (e.g. Dobbs & Bonnell 2007; Dekel et al. 2009; Ceverino et al. 2010; Aumer et al. 2010; Oliva-Altamirano et al. 2018). In this paper, we will be focusing primarily on differentiating star-formation feedback processes and gravitational transport of gas through the disc due to the clear predictions that have been made in the integrated star-formation rate (SFR) and global velocity dispersion (σ_v) plane (Krumholz & Burkart 2016; Krumholz et al. 2018).

Star-formation feedback is thought to be dominated by the energy imparted by supernovae (Norman & Ferrara 1996; Mac Low & Klessen 2004). However, other drivers such as stellar winds, expansion of H II regions (Chu & Kennicutt 1994; Matzner 2002), and radiation pressure in high density star clusters (Krumholz & Matzner 2009; Murray et al. 2010) will also inject momentum into the interstellar medium. Observational evidence for star-formation feedback as the primary driver of gas turbulence has been argued by observing that SFR is

correlated with σ_v. The SFR $– \sigma_v$ correlation has been shown both within a single sample at constant redshift (Green et al. 2010, 2014; Moiseev et al. 2015; Yu et al. 2019) and by combining multiple samples across epochs (Green et al. 2010, 2014).

Assuming that star-formation feedback processes are a significant driver of the turbulence, it would be natural to expect a relation between local star-formation rate surface density (Σ_{SFR}) and local velocity dispersion. There are conflicting results in the literature regarding the relationship between these local quantities. Some studies have found a significant relationship (Lehnert et al. 2009, 2013), whereas others have found the localised relationship to be weak (Genzel et al. 2011; Varidel et al. 2016; Zhou et al. 2017; Übler et al. 2019).

Furthermore, the physical mechanism for an energetic source to account for velocity dispersions due to star-formation feedback of several tens of km s^{-1} is not well established. Constructing equilibrium solutions between gravitational infall of the disc supported by outward pressure solely by supernovae leads to $\sigma_v \lesssim 25$ km s^{-1} with little variation as a function of SFR (Ostriker & Shetty 2011; Krumholz et al. 2018). An alternative approach that can account for increased turbulence is to assume that the star-formation efficiency per free-fall time (ϵ_{ff}) changes as a function of galaxy properties, thus changing the energetic input from star-formation feedback processes (Faucher-Giguère et al. 2013). However, numerous observations suggest that ϵ_{ff} is approximately constant across a wide range of galaxy properties (Krumholz & Tan 2007; Krumholz et al. 2012; Federrath 2013; Salim et al. 2015; Krumholz et al. 2019).

An alternative set of driving mechanisms are due to gravitational effects. This includes the initial gravitationally unstable formation of the disc (Aumer et al. 2010), that can account for short-lived supersonic turbulence on the order of the disc formation time, $\mathcal{O}(100 \text{ Myr})$. It is thought that the supersonic turbulence that is initially set at disc formation can be maintained by the gravitational transport of gas through the disc (Krumholz & Burkert 2010). Krumholz & Burkhart (2016) also argued that the gravitational transport model predicts an increase in velocity dispersion at increased SFR that is more consistent with the data than models assuming star-formation feedback processes.

A further complication involved in inferring the ongoing drivers of turbulence across epochs is the effects of the spectral and spatial resolution on the observed velocity dispersion. The spectral resolution broadens the observed emission line often on order of the intrinsic velocity dispersion. This is typically accounted for by convolving the modelled emission line profile by the known Line-Spread Function (LSF) while fitting to the data (e.g. Förster Schreiber et al. 2009; Davies et al. 2011; Green et al. 2014; Varidel et al. 2019). This is a reasonable approximation as long as the model assumptions regarding the LSF are well known.

The spatial resolution is more difficult to account for as it acts to blur the emission line flux spatially per spectral slice. The observed velocity dispersion is then a complex function of the intrinsic flux distribution, line of sight (LoS) velocity profile, and LoS velocity dispersion profile. This effect is usually referred to as beam smearing.

In general, beam smearing acts to increase the observed velocity dispersion particularly where the velocity gradient is

steepest (Davies et al. 2011; Glazebrook 2013), and in detail can result in spurious substructure in the velocity dispersion profile (Varidel et al. 2019). Furthermore, beam smearing could result in spurious correlations such as the SFR – σ_v correlation, as SFR is related to the mass which shapes the gravitational potential, and thus increases the velocity gradient at the centre of galaxies with higher SFR. Similarly, the width of the Point-Spread Function (PSF) relative to the galaxy size increases for increasing z, thus resulting in higher observed velocity dispersions if beam smearing is not corrected for appropriately.

The SFR – σ_v relation has been used to distinguish between the different energetic sources of turbulence (Krumholz & Burkhart 2016; Krumholz et al. 2018). However, comparisons between theoretical models and observations have typically been performed by combining several studies with different redshift ranges and beam smearing corrections. In this paper, we improve comparisons of the observed velocity dispersion to theoretical models by studying a sample of nearby galaxies using a single technique to mitigate the effects of beam smearing. The data encompasses a wide range of SFR $\in [10^{-3}, 10^2]$ M$_\odot$ yr^{-1} of local galaxies at $z \lesssim 0.1$. The combined sample is comprised of observations from the SAMI Galaxy Survey Data Release Two (SAMI Galaxy Survey DR2, Croom et al. 2012; Scott et al. 2018) and the DYNAMO survey (Green et al. 2014). We use a consistent disc-fitting routine referred to as BLOBBY3D (Varidel et al. 2019), for all the galaxy gas kinematic modelling in this paper. BLOBBY3D is a disc fitting code that constructs a regularly rotating thin-disc galaxy model in 3D (position – position – wavelength space) that is then convolved by the PSF and LSF prior to comparing the model to the data. In that way it can account for the effect of beam smearing when inferring the velocity dispersion of the galaxy.

The outline of this paper is as follows. In Section 2 we describe the SAMI Galaxy Survey and DYNAMO surveys, as well as our sample selection criteria. In Section 3 we outline the methods used to measure the key gas kinematic properties. In Section 4, we will discuss our results. In Section 5 we compare our results to theoretical models of the drivers for turbulence. We summarise our conclusions in Section 6. Throughout this paper we assume the concordance cosmology ($\Omega_\Lambda = 0.7$, $\Omega_m = 0.3$, $H_0 = 70$ km s^{-1} Mpc^{-1}; Hinshaw et al. 2009) and a Chabrier (2003) Initial Mass Function (IMF).

2 DATA SELECTION

2.1 The SAMI Galaxy Survey

The SAMI Galaxy Survey was conducted with the Sydney-AAO Multi-object Integral field Spectrograph (SAMI, Croom et al. 2012). SAMI was mounted at the Anglo-Australian Telescope (AAT), that provided a 1 degree diameter Field-of-View (FoV). SAMI used 13 fused fibre bundles, known as Hexabundles (Bland-Hawthorn et al. 2011; Bryant et al. 2014), with a 75% fill factor. Each bundle contains 61 fibres of 1.6″ diameter, resulting in an approximately 15″ diameter FoV. The IFUs as well as 26 sky fibres were attached to pre-drilled plates using magnetic connectors. SAMI fibres were fed to the double-beam AAOmega spectrograph (Sharp et al. 2006). The 580V grating at 3750–5750 Å provides a

resolution of $R = 1808$ ($\sigma = 70.4$ km s^{-1} at 4800 Å) and the 1000R grating from 6300–7400 Å providing a resolution of $R = 4304$ ($\sigma = 29.6$ km s^{-1} at 6850 Å) (Scott et al. 2018).

During the survey, observations of over 3000 galaxies were obtained. Target selection for the SAMI Galaxy Survey are provided in Bryant et al. (2015). The redshift range for the observed galaxies was $0.004 < z < 0.113$ and a stellar mass range of $7.5 < \log(M_*/M_\odot) < 11.6$. The Full-Width Half-Maximum (FWHM) of the seeing distribution was $1.10'' <$ FWHM$_{\rm PSF} < 3.27''$. Relevant data used for the analysis in this paper are from the SAMI Galaxy Survey DR2 (Scott et al. 2018). This includes the aperture spectra, emission line products (Green et al. 2018), data cubes (Sharp et al. 2015), and input catalogue (Bryant et al. 2015).

2.2 Sample selection from the SAMI Galaxy Survey

Our aim was to select galaxies on the star-forming main sequence within the SAMI Galaxy Survey. As such, we performed the following selection criteria cuts to the sample from the SAMI Galaxy Survey DR2 (Scott et al. 2018).

Star-forming galaxies are selected by applying a cutoff integrated Hα equivalent width of $EW > 3$ Å (Cid Fernandes et al. 2011). The equivalent width is calculated as the total Hα flux compared to the total continuum flux across the SAMI FoV. The continuum flux in the region around Hα is estimated by calculating the mean continuum in the wavelength range [6500, 6540] Å. The integrated Hα flux estimates is sourced from the SAMI Galaxy Survey DR2 emission line data products.

We remove galaxies with ionised emission from non star-forming sources such as Active Galactic Nuclei (AGN) and Low-Ionisation Nuclear Emission-line Regions (LINERs). To implement this criteria, we remove galaxies where the AGN classification criteria proposed by Kauffmann et al. (2003) is met,

$$\log([\text{O III}]/\text{H}\beta) > \frac{0.61}{\log([\text{N II}]/\text{H}\alpha) - 0.05} + 1.3. \qquad (1)$$

[O III] and [N II] represent the emission line fluxes at 5007 Å and 6583 Å, respectively. The line fluxes are estimated for the central region of the galaxy where AGN and LINER contamination should be greatest, using the $1.4''$ aperture spectra from the SAMI Galaxy Survey DR2.

We retain galaxies that are face-on up to $e = 1 - b/a = 0.5$ ($0° < i < 60°$, assuming a thin disc). We avoid galaxies observed at high inclination as the intrinsic velocity dispersion is more difficult to constrain due to beam smearing. Plus galaxies are optically thick such that edge-on observations limit the ability to observe the integrated LoS from the entire galaxy. Furthermore, a thin disc model is assumed in BLOBBY3D, such that the galaxies will not be well modelled when observed close to edge-on.

We apply the following signal-to-noise cut on the spaxels in the data. We first apply a mask to spaxels with Hα flux signal-to-noise < 3. Spatially resolved Hα flux and it's error are obtained from the SAMI Galaxy Survey DR2 pipeline. We then construct groups of unmasked spaxels that are adjacent and meet the signal-to-noise criteria. The largest unmasked group is retained, whereas the remaining spaxels are masked. We retain galaxies that had at least 300 unmasked spaxels.

The above masking routine only finds the largest group of spaxels, which in principle could reject clumpy flux profiles. In practice, the effect of removing Hα clumps originating from the galaxy was negligible. Instead, it primarily removed spurious spaxels that were reported to have high signal-to-noise, yet by eye did not appear to be legitimate detections of flux originating from the galaxy.

We also remove mergers or galaxies with clearly disturbed gas kinematics from our final sample. Potential mergers were determined by eye from observations of the gas kinematic maps. 9 galaxies were removed from our final sample due to this criteria.

There are 1523 galaxies in the SAMI Galaxy Survey DR2 where all of the above diagnostic criteria are measurable. 342 galaxies remain once our criteria is applied. Figure 1 shows that we are selecting galaxies along the star-forming main sequence. We see a clear bimodal distribution in the log equivalent width, where we have selected those galaxies with $EW > 3$ Å. The equivalent width cut removes massive galaxies that are typically passive, which can be seen when plotting the equivalent width compared to M_* and R_e. There are a limited number of galaxies in our sample with 3 Å $< EW \lesssim 10$ Å as many of those galaxies are removed due to being classified as LINER/AGN or having < 300 spaxels that meet our signal-to-noise masking criteria.

Removing highly inclined galaxies results in a large cut to our sample, but does not bias our sample along any galaxy properties. Also, the selection of galaxies with at least 300 unmasked spaxels does remove galaxies with $R_e \lesssim 1''$, but there are very few of these galaxies in the underlying SAMI Galaxy Survey DR2 sample.

2.3 DYNAMO sample

The DYnamics of Newly Assembled Massive Objects (DYNAMO, Green et al. 2014) survey consists of a sample of star-forming galaxies in the local Universe ($z \lesssim 0.1$). These galaxies were classified as star-forming in the MPA-JHU Value Added Catalog from the Sloan Digital Sky Survey (SDSS, York et al. 2000). The galaxies comprising the DYNAMO survey were chosen primarily based on Hα luminosity. The aim was to include both high Hα luminous galaxies, that are rare in the local Universe, as well as a sample of typical galaxies in the local Universe. The resulting galaxy sample ranged SFR $\in [1, 100]$ $M_\odot$ yr^{-1}.

The data for the DYNAMO samples was obtained via observations using the 3.9 m Anglo-Australian Telescope (AAT) and the ANU 2.3 m Telescope at Siding Spring Observatory. The AAT was equiped with the SPIRAL Integral-Field Unit (IFU) with the AAOmega Spectrograph (Sharp et al. 2006). SPIRAL is an array of 32×16 square, $0.7''$ lenslets with a contiguous integral field of $22.4'' \times 11.2''$. The 1700I grating was used on the red spectrograph providing a nominal resolution power of $R \sim 12000$. The ANU 2.3 m Telescope was equiped with the Wide-Field Spectrograph (WiFeS, Dopita et al. 2007). WiFeS has a $25'' \times 38''$ FoV with either $1.0'' \times 0.5''$ or $1.0'' \times 1.0''$ spaxels. The I7000 grating was chosen for the red arm, which has a $6893-9120$ Å wavelength range with a spectral resolving power of $R \sim 7000$.

A total of 67 galaxies comprised the original DYNAMO sample. We remove galaxies observed at $i > 60°$, where i has been measured using the SDSS photometric pipeline using

an exponential disc fit to the r-band. We perform the same masking criteria as described for the galaxies from the SAMI Galaxy Survey. We also remove galaxies with less than 30 unmasked spaxels. 41 galaxies were retained from the original DYNAMO sample.

3 METHODS

3.1 Modelling the gas disc kinematics

We use Blobby3D (Varidel et al. 2019) to infer the intrinsic gas kinematics for the observed galaxies. Blobby3D is a forward-fitting disc modelling procedure. It assumes that the gas lies in a regularly rotating thin-disc. The prior for the spatial gas distribution within the disc allows for clumpy gas profiles using a hierarchical Gaussian mixture-model. The model is constructed in 3D (position – position – wavelength space) and then convolved in accordance with the PSF and instrumental broadening by the LSF. The convolved model is then compared to the observed data cube.

The advantage of Blobby3D is that it is capable of performing inference for the spatial gas distribution, including substructure, plus the gas kinematics simultaneously. This is important as the effect of beam smearing is a function of the spatial gas distribution being blurred per spectral slice. As such, the observed gas kinematics is a complex function of the intrinsic spatial gas distribution, the velocity profile, and the velocity dispersion plus instrumental broadening and beam smearing. For example, Varidel et al. (2019) found that it is possible to observe spurious substructure in the gas kinematics in a symmetric regularly rotating disc with an asymmetric spatial gas distribution plus beam smearing.

Previous testing of Blobby3D has found that it is well optimised to infer the intrinsic velocity dispersion of galaxies (Varidel et al. 2019). Blobby3D was compared to an alternative forward-fitting methodology known as ^{3D}Barolo (Di Teodoro & Fraternali 2015). It was also compared to other heuristic modelling approaches that have been used in the literature, such as estimating the velocity dispersion in the outskirts of the galaxy (e.g. Zhou et al. 2017), correcting the observed velocity dispersion as a function of the velocity gradient (e.g. Varidel et al. 2016), and subtracting the velocity gradient in quadrature from the observed velocity dispersion (e.g. Oliva-Altamirano et al. 2018). Blobby3D was found to infer the intrinsic velocity dispersion more accurately than these alternative methods, particular for galaxies where the PSF or velocity gradient were greatest.

The parameterisation for Blobby3D is set within the Bayesian framework. The joint prior distribution for the parameters, hyperparameters, and data were defined in Varidel et al. (2019). We only make minor changes to the priors that were previously proposed. We outline the motivation for changing some of the prior distributions below.

The joint prior distribution used for this work performs inferences for the Hα flux plus the [N II]/Hα emission flux ratio for each spatial Gaussian flux profile (often referred to as a 'blob' in Blobby3D). The gas kinematics have been assumed to be consistent across the different gas components. Therefore, the inferences for the kinematics are constrained using extra information from the [N II] emission lines at 6548.1 Å and 6583.1 Å. The ratio of the flux between the [N II] emission lines is assumed to be $F_{6583.1}/F_{6548.1} = 3$.
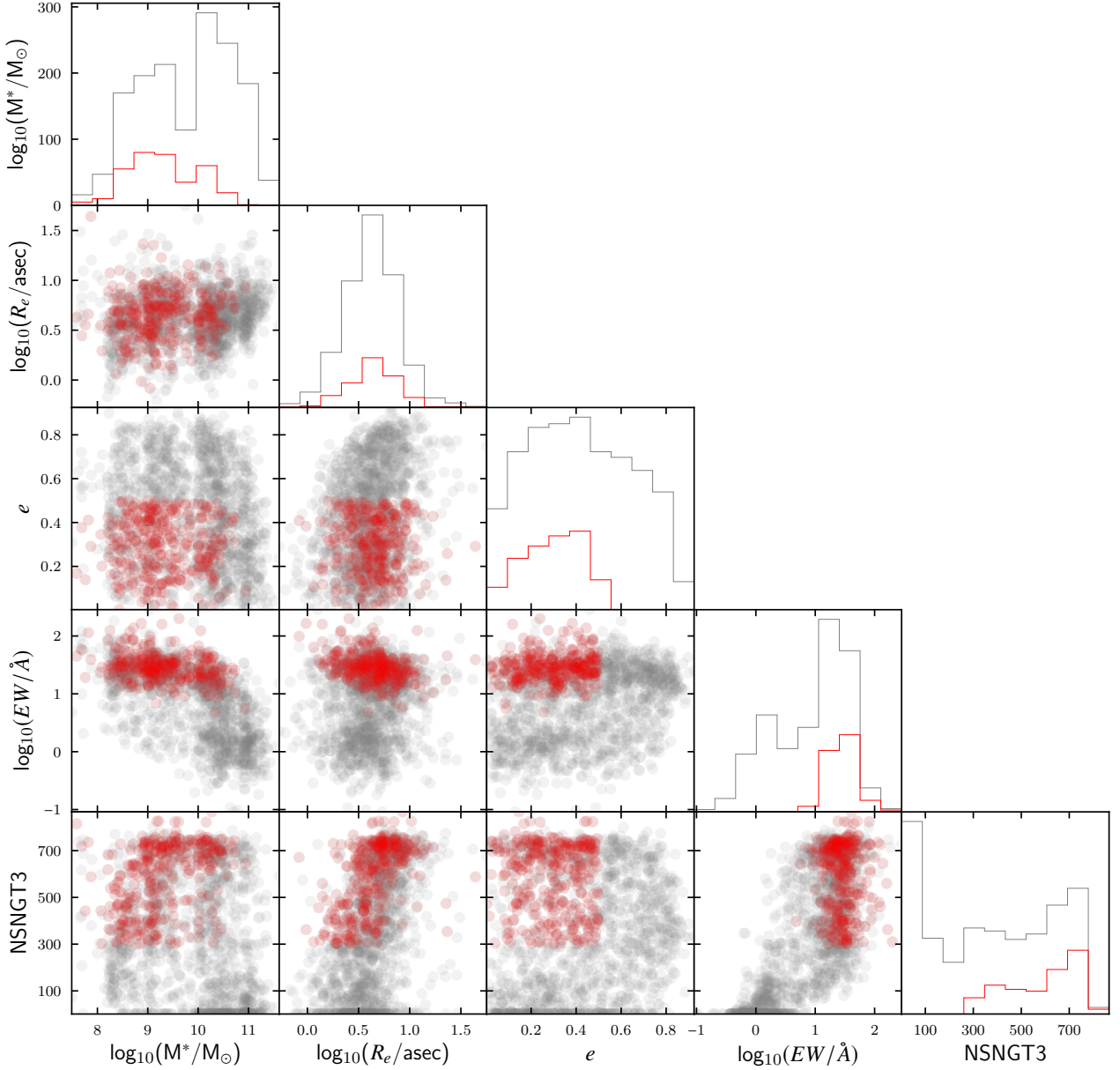
Figure 1. Galaxy parameters for our sample of 342 galaxies (red) selected from the total SAMI Galaxy Survey (grey). We show the marginalised (diagonal) and conditional (off-diagonal) distributions for the stellar mass ($\log_{10}(M^*/M_\odot)$), effective radius ($\log_{10}(R_e/\text{asec})$), ellipticity ($e = 1 - b/a$), H$\alpha$ equivalent width ($\log_{10}(EW/\text{Å})$), and NSNGT3. NSNGT3 corresponds to the number of spaxels that meet our signal-to-noise masking criteria. We select a sample of star-forming galaxies from the SAMI Galaxy Survey with inclination and signal-to-noise cuts that can be adequately modelled using Blobby3D.

To simplify the inference for the velocity dispersion, we assume a constant velocity dispersion across the disc ($\sigma_{v,0}$). We assume no radial gradient as the results for some galaxies returned large positive gradients when using the prior suggested by Varidel et al. (2019). The large spatial gradients in velocity dispersion after convolution appeared to be over-fitting for wider-tailed non-Gaussian emission line profiles. Therefore, we removed the velocity dispersion

gradient from the inference in order to robustly infer the constant velocity dispersion component for the large sample of galaxies that were studied in this work.

We have also widened the bounds for our priors for the systemic velocity (v_{sys}) and the asymptotic velocity (v_c) in order to model a larger set of galaxies than was performed

by Varidel et al. (2019). Our new priors are,

$$v_{\mathrm{sys}} \sim \mathrm{Cauchy}(0, 30 \text{ km s}^{-1})T(-300 \text{ km s}^{-1}, 300 \text{ km s}^{-1}), \quad (2)$$

$$v_c \sim \mathrm{Loguniform}(1 \text{ km s}^{-1}, 1000 \text{ km s}^{-1}). \quad (3)$$

Where $T(a, b)$ represents the distribution being truncated to the interval $[a, b]$.

3.1.1 Mitigating the effects of beam smearing

The effect of beam smearing by the PSF is accounted for in BLOBBY3D by convolving the underlying model constructed by the PSF, prior to calculating the likelihood function. The PSF profile assumed in BLOBBY3D is a superposition of 2D concentric circular Gaussian profiles. Therefore, the PSF needs to first be modelled assuming this flux profile.

The SAMI Galaxy Survey pipeline provides estimates for the PSF by fitting a profile to a star that was observed simultaneously with the galaxy. We have used the Moffat profile estimates, where the PSF is described as,

$$p(r) = \frac{\beta - 1}{\pi \alpha^2} \left(1 + \frac{r^2}{\alpha^2}\right)^{-\beta}. \quad (4)$$

α is the FWHM and β is a shape parameter that controls the tails of the Moffat profile.

To refactor the Moffat profile parameters into a set of concentric Gaussians, we construct the 1D Moffat profile, then fit it with two 1D Gaussians. Two Gaussians were enough to adequately model the PSF profile. The estimated Gaussian parameters are then passed to BLOBBY3D.

For the DYNAMO sample, the FWHM of the PSF was measured during observations. As such, we assumed a 2D circular Gaussian profile to be representative of the PSF for the DYNAMO sample. Thus, the underlying model in BLOBBY3D was convolved with a Gaussian profile prior to comparing the model to the data for our galaxies from the DYNAMO survey.

3.1.2 Continuum substraction

BLOBBY3D requires the data to be continuum subtracted. For galaxies from the SAMI Galaxy Survey, we use the continuum models made available in the SAMI Galaxy Survey DR2 pipeline. The full description for the continuum modelling routine is described in Owers et al. (2019). We estimate the continuum for the galaxies from the DYNAMO survey using a 300 bin moving median filter as also implemented by Green et al. (2014).

It is possible for the continuum modelling to introduce systematics in the resulting continuum subtracted data cube. These systematics may not be well accounted for in the BLOBBY3D approach. We make the assumption that the stellar continuum will be adequately modelled in regions of high Hα signal-to-noise. This is a significant motivation for implementing the Hα signal-to-noise masking outlined in Section 2.2.

3.1.3 Posterior optimisation

We use DNEST4 (Brewer et al. 2011; Brewer & Foreman-Mackey 2018) to get a point estimate of the maxima for the posterior PDF. DNEST4 is a sampling algorithm based on

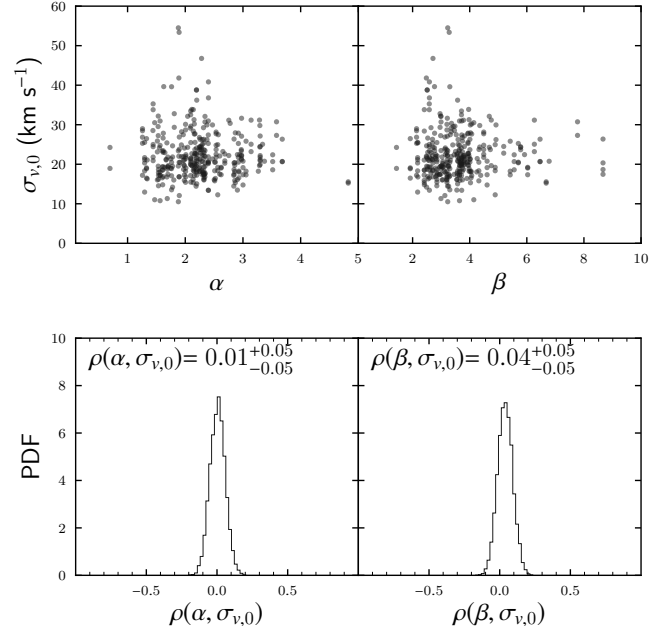**Figure 2.** Comparing the PSF Moffat profile parameters α and β to the inferred global velocity dispersion for galaxies in our sample from the SAMI Galaxy Survey. We also show the PDF of the Spearman-rank correlation coefficients estimated using 10^4 bootstrap samples (bottom). $\rho = 0$ lies within the 68% shortest credible intervals suggesting that $\sigma_{v,0}$ is adequately corrected for beam smearing.

nested sampling (Skilling 2004), where the new levels are constructed by exploring a weighted mixture of the previous levels. Exploration of the levels is performed using a Metropolis Markov Chain Monte Carlo (MCMC). The multi-level exploration allows DNEST4 to be significantly more robust to local maxima compared to typical nested sampling, allowing for the exploration of high parameter spaces and multi-modal posterior distributions. Estimated values throughout this paper are of the maximum posterior PDF value in the chain sampled using DNEST4.

3.2 Global velocity dispersion

3.2.1 Beam smearing corrections

Assuming that BLOBBY3D accurately corrects for beam smearing, there should be no residual correlation between the PSF profile parameters and the inferred intrinsic velocity dispersion ($\sigma_{v,0}$). The distribution of $\sigma_{v,0}$ is consistent with our expectations for a beam smearing corrected sample. Figure 2 shows a comparison between the PSF Moffat profile parameters and $\sigma_{v,0}$ for our sample from the SAMI Galaxy Survey. For both α and β, zero remains inside the 68% shortest credible intervals for the Spearman-rank correlation coefficients.

For galaxies from the DYNAMO survey, the Spearman-rank correlation coefficient is estimated as $\rho(\mathrm{FWHM}, \sigma_v) = 0.10^{+0.17}_{-0.17}$. As zero remains within the 68% confidence interval, this result is also consistent with a beam smearing corrected sample.

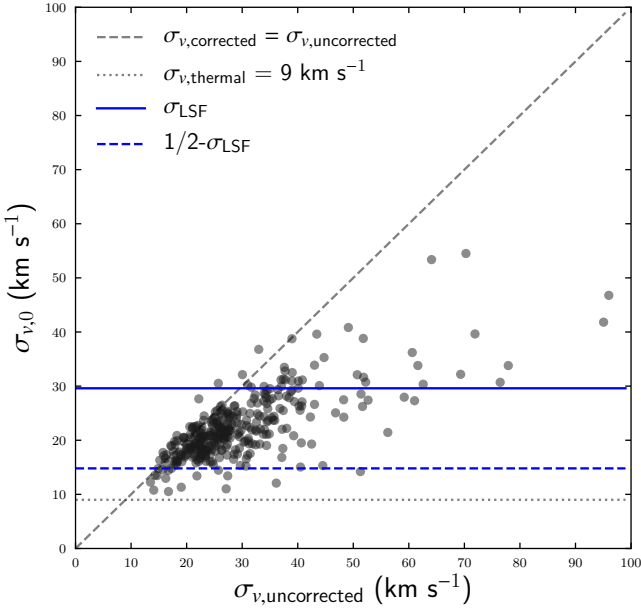We also compare $\sigma_{v,0}$ to an estimate of the veloc-

Figure 3. $\sigma_{v,0}$ estimated using BLOBBY3D compared to the arithmetic mean of the single-component fits per spaxel ($\sigma_{v,\text{uncorrected}}$) to each galaxy from the SAMI Galaxy Survey sample. Estimates for the velocity dispersion are typically lower using BLOBBY3D as it mitigates the effects of beam smearing.

ity dispersion that was not corrected for beam smearing ($\sigma_{v,\text{uncorrected}}$). The uncorrected estimator is calculated as the arithmetic mean velocity dispersion across the FoV, when fitting a single Gaussian component to each spaxel. Spaxels with Hα signal-to-noise < 3 are masked in this process to eliminate the effects of poorly constrained spaxels on the final estimate.

Estimates for $\sigma_{v,0}$ are significantly lower than $\sigma_{v,\text{uncorrected}}$ (see Figure 3). Using the sample of galaxies from the SAMI Galaxy Survey, typical corrections were $\Delta\sigma_v = -5.3^{+4.0}_{-7.0}$ km s^{-1} and $\Delta\sigma_v/\sigma_{v,0} = -0.20^{+0.14}_{-0.18}$, where $\Delta\sigma_v = \sigma_{v,0} - \sigma_{v,\text{uncorrected}}$. The typical beam smearing corrections are consistent with the results found by Varidel et al. (2019) on a sample of 20 star-forming galaxies in the SAMI Galaxy Survey using BLOBBY3D.

All estimated values have $\sigma_{v,0} > \sigma_{v,\text{thermal}} = 9$ km s^{-1}. $\sigma_{v,\text{thermal}}$ is the typical emission line width expected for a H II region at $\sim 10^4$ K (Glazebrook 2013). As such, $\sigma_{v,\text{thermal}}$ sets a physically motivated lower bound.

3.2.2 Considerations of the effects of the LSF on the velocity dispersion estimates

The SAMI instrument has the spectral resolution of $\sigma_{\text{LSF}} = 0.68$ Å ($\sigma_{v,\text{LSF}} = 29.6$ km s^{-1}) in the red arm. For reference, we show the 1-$\sigma_{v,\text{LSF}}$ and 1/2-$\sigma_{v,\text{LSF}}$ on Figure 3. 89% of our galaxies have estimated intrinsic velocity dispersions less than $\sigma_{v,\text{LSF}}$ and 4.6% of our sample were estimated to have intrinsic velocity dispersion less than $\sigma_{v,\text{LSF}}/2$.

We correct for the LSF by convolving the emission line by a Gaussian profile with $\sigma_{v,\text{LSF}}$ during the fitting procedure in BLOBBY3D. This procedure assumes that the observed emission line is a convolution of two Gaussians. Therefore,

the estimated velocity dispersion can be affected by non-Gaussianities in the shape of the LSF, particularly when the velocity dispersion is significantly less than the width of the LSF. However, deviations of the SAMI LSF from a Gaussian profile are minor (van de Sande et al. 2017). Also 95.4% of our sample were estimated to be $\sigma_{v,0} > \sigma_{v,\text{LSF}}/2$, as such the effects of minor systematic differences of the LSF from a Gaussian profile is unlikely to have significant effects on our inferences.

Similarly, the effect of variations in the LSF FWHM are minor for the SAMI Galaxy Survey. The LSF FWHM varied at the ~5% level as a function of fibre, time, and wavelength during the SAMI Galaxy Survey (Scott et al. 2018). For the velocity dispersions values that we estimate, this should result in uncertainties on the level of $\Delta\sigma_v \sim 1$ km s^{-1}. As such, the variation of the LSF FWHM is not expected to have any significant effect on the conclusions drawn in this paper.

3.2.3 Estimating the vertical velocity dispersion

Our disc modelling approach calculates a global estimate for the intrinsic line-of-sight (LoS) velocity dispersion ($\sigma_{v,0} \equiv \sigma_{v,\text{LoS}}$). Most studies using IFS observations report $\sigma_{v,\text{LoS}}$. However, $\sigma_{v,\text{LoS}}$ is a mixture of the radial ($\sigma_{v,R}$), azimuthal ($\sigma_{v,\phi}$), and vertical ($\sigma_{v,z}$) velocity dispersion components.

At any point in the sky, $\sigma_{v,\text{LoS}}$ is given by (e.g. Equation 27a, Cappellari 2019),

$$\sigma_{v,\text{LoS}}^2 = (\sigma_{v,R}^2 \sin^2\phi + \sigma_{v,\phi}^2 \cos^2\phi)\sin^2 i + \sigma_{v,z}^2 \cos^2 i. \quad (5)$$

Observed $\sigma_{v,\text{LoS}}$ is the luminosity-weighted integral along the LoS. To calculate the average velocity dispersion, we make the following approximations. We assume that the flux is constant across a thin disc with finite radial extent. We also assume spatially constant velocity dispersion components and that $\sigma_{v,\perp}^2 \equiv \sigma_{v,R}^2 \approx \sigma_{v,\phi}^2$ then the average LoS velocity dispersion is given by,

$$\bar{\sigma}_{v,\text{LoS}}^2 = \sigma_{v,\perp}^2 \sin^2 i + \sigma_{v,z}^2 \cos^2 i. \quad (6)$$

Setting $\gamma^2 = \sigma_{v,z}^2/\sigma_{v,\perp}^2$, and rearranging, then

$$\sigma_{v,\text{LoS}} = \sigma_{v,z}\sqrt{\sin^2 i/\gamma^2 + \cos^2 i} \quad (7)$$

The above model predicts changing $\sigma_{v,\text{LoS}}$ as a function of i if $\gamma \neq 1$. For $\gamma > 1$, $\sigma_{v,\text{LoS}}$ increases with increasing i, whereas $\sigma_{v,\text{LoS}}$ decreases with i when $\gamma < 1$.

To estimate γ we assume that $\sigma_{v,\text{LoS}}$ follows a loguniform distribution with mean $\sigma_{v,z,0}$ and log variance τ^2. The generating function for a single data point $\sigma_{v,z,i}$ is then,

$$p(\sigma_{v,\text{LoS},j}|\sigma_{v,z,0},\tau^2,\gamma) \sim \text{lognormal}(\sigma_{v,z,0}\sqrt{\sin^2 i/\gamma^2 + \cos^2 i},\tau^2). \quad (8)$$

We assume the following priors,

$$p(\sigma_{v,z,0}) \sim \text{loguniform}(1,100) \quad (9)$$

$$p(\tau) \sim \text{loguniform}(10^{-3},1) \quad (10)$$
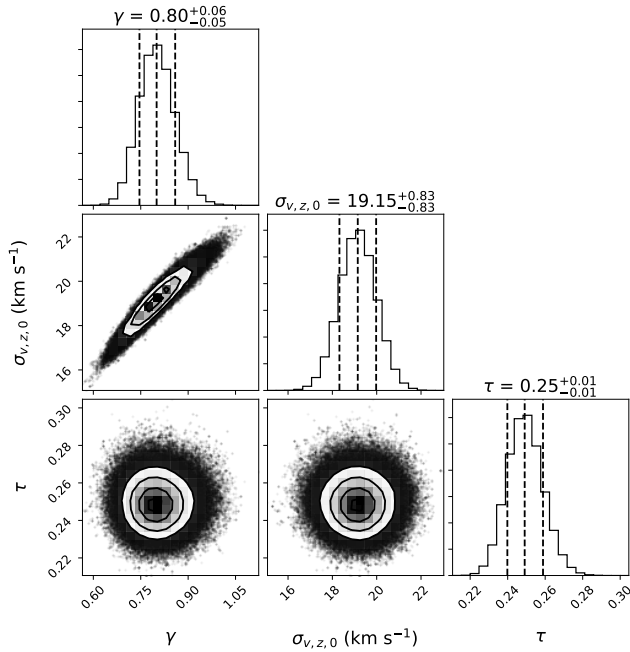
$$p(\gamma) \sim \text{loguniform}(0.1,10). \quad (11)$$

Figure 4. Corner plot (Foreman-Mackey 2016) showing the marginalised (diagonal) and joint (off-diagonal) posterior distributions for the parameter estimation for the inclination dependence model. There is evidence for a dependence of $\sigma_{v,\text{LoS}}$ on inclination for our sample of galaxies from the SAMI Galaxy Survey. This suggests that the vertical velocity dispersion ($\sigma_{v,z}$) is less than the averaged azimuthal and radial velocity dispersion ($\sigma_{v,\perp}$).

The posterior distribution is then given by,

$$p(\sigma_{v,z0}, \tau, \gamma | \mathbf{D}) = p(\sigma_{v,z,0}) p(\tau) p(\gamma) \prod_{j=1}^{N} p(\sigma_{v,\text{LoS},j} | \sigma_{v,z,0}, \tau^2, \gamma). \tag{12}$$

The above formulation assumes independence of the prior distribution between $\sigma_{v,z,0}$, τ, γ, as well as all $\sigma_{v,\text{LoS},j}$. The above posterior distribution can now be sampled using typical techniques. We used EMCEE to sample the posterior distribution (Foreman-Mackey et al. 2013).

We estimate $\gamma = 0.80^{+0.06}_{-0.05}$ as shown in Figure 4, suggesting that the vertical velocity dispersion is less than the averaged azimuthal and radial components. This analysis was consistent with other approaches that we applied. For example, the bootstrapped Spearman-rank correlation coefficient distribution between the inclination and $\sigma_{v,\text{LoS}}$ was $\rho(i, \sigma_{v,\text{LoS}}) = 0.18^{+0.05}_{-0.05}$, where the uncertainties for the Sperman-rank correlation coefficient is estimated as the 68% shortest credible interval after bootstrap resampling. We also performed the above analysis using uniform priors for $\sigma_{v,z,0}$ and γ with the same ranges, yet we still find $\gamma = 0.80^{+0.06}_{-0.06}$.

Previous studies have suggested that $\sigma_{v,z}/\sigma_{v,R} \sim 0.6$ (Section 1.2.2, Glazebrook 2013) for stars. Mean H I gas velocity dispersion was reported up to ~ 3 times higher for galaxies observed at $i > 60°$ compared to $i < 60°$ by Leroy et al. (2008), also suggesting that the contribution of $\sigma_{v,R}$ and $\sigma_{v,\phi}$ dominates.

Studies of gas kinematics have typically not reported or found evidence that $\sigma_{v,z}$ is related to the inclination. For
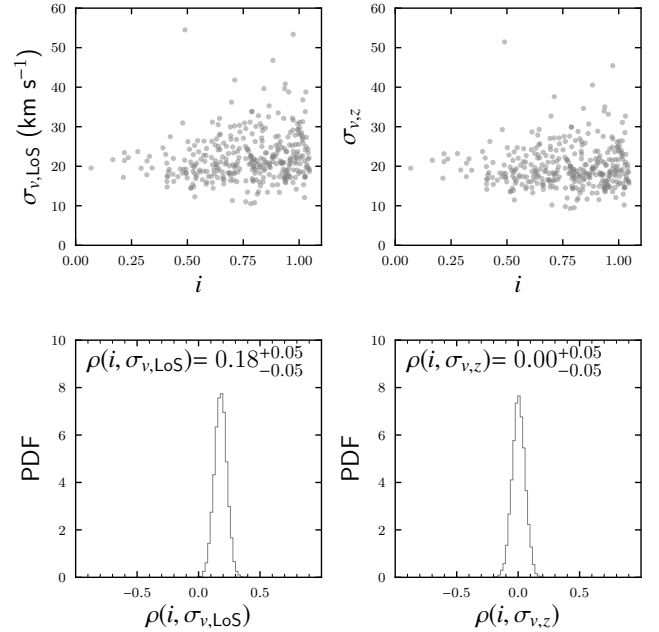

Figure 5. The relationship between the inclination (i) and inferred velocity dispersion estimates. We also show the PDF of the Spearman-rank correlation coefficients using bootstrap resampling (bottom). There is evidence for a weak positive correlation between the LoS velocity dispersion $\sigma_{v,\text{LoS}}$ and i. Whereas the distribution for the vertical velocity dispersion after applying a correction factor yields no relation with i.

example, studies of high-z in the KMOS3D Survey have found no significant correlation between the axis ratio $q = b/a$ and $\sigma_{v,\text{LoS}}$ (Wisnioski et al. 2015; Übler et al. 2019). However, such a relation may be difficult to identify in high-z galaxies with lower signal-to-noise and spatial resolution.

We estimate the vertical velocity dispersion ($\sigma_{v,z}$) for individual galaxies by inverting Equation 7 and using $\gamma = 0.8$. We estimated the Spearman-rank correlation between the inclination and $\sigma_{v,z}$ to be $\rho(i, \sigma_{v,z}) = 0.00^{+0.05}_{-0.05}$ after performing the correction per galaxy, suggesting that our analysis appropriately removed the correlation as a function of the inclination angle.

Converting from $\sigma_{v,\text{LoS}}$ to $\sigma_{v,z}$ adjusts the reported values by a couple of km s^{-1}. The marginalised distributions yield $\sigma_{v,\text{LoS}} = 21.1^{+3.9}_{-5.2}$ km s^{-1} and $\sigma_{v,z} = 18.8^{+3.4}_{-4.8}$ km s^{-1} (see Figure 6). Typical differences are $\sigma_{v,\text{LoS}} - \sigma_{v,z} = 2.4^{+0.9}_{-1.3}$ km s^{-1}, with the greatest correction being $\sigma_{v,\text{LoS}} - \sigma_{v,z} = 7.9$ km s^{-1}.

For the remainder of this paper, we will report the values of $\sigma_{v,z}$. The subsequent analysis and results do not change qualitatively whether we use $\sigma_{v,z}$ or $\sigma_{v,\text{LoS}}$, but $\sigma_{v,z}$ is preferred as it is an estimator free from effects from the viewing angle. It is also more appropriate to compare $\sigma_{v,z}$ to theoretical models, as they are typically framed with respect to $\sigma_{v,z}$. We report both values in Appendix A.

We have not applied the inclination correction for galaxies observed in the DYNAMO survey. This is due to finding no significant relation with $\rho(i, \sigma_{v,\text{los}}) = -0.09^{+0.15}_{-0.15}$ for our galaxies from the DYNAMO survey. This suggests that there is no inclination effect to correct for within this sample. It
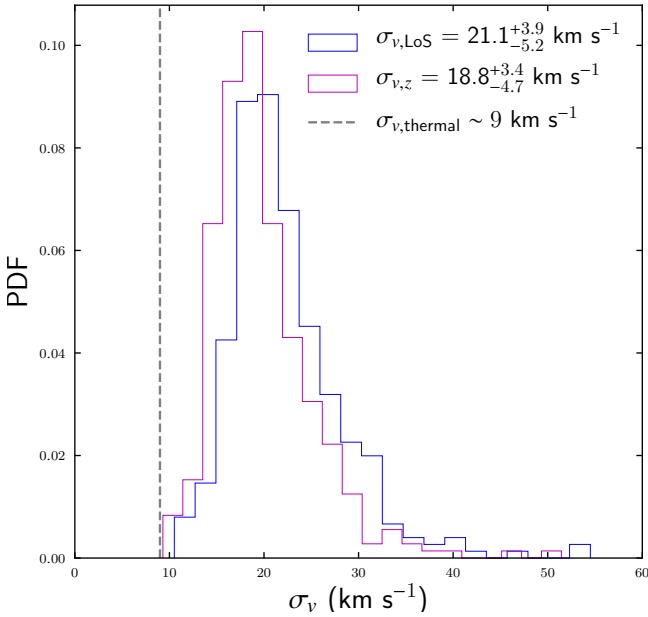
Figure 6. The distribution of the LoS ($\sigma_{v,\mathrm{LoS}}$, blue) and vertical ($\sigma_{v,z}$, red) velocity dispersion for our sample of galaxies from the SAMI Galaxy Survey. The estimated vertical velocity dispersion is adjusted down with respect to $\sigma_{v,\mathrm{LoS}}$ by a couple of km s^{-1} in accordance with the inclination correction described in Section 3.2.3.

may be that the sample from the DYNAMO survey is too small to infer the inclination effect. In this case, we choose not to apply the inclination effect found from the SAMI Galaxy Survey, as it is still possible that the inferred effect is methodological rather than physical across all galaxies.

3.3 Circular velocity estimates

Blobby3D estimates the LoS velocity profile using the empirical model proposed by Courteau (1997),

$$v(r) = v_\mathrm{c} \frac{(1 + r_t/r)^\beta}{(1 + (r_t/r)^\gamma)^{1/\gamma}} \sin(i)\cos(\theta) + v_\mathrm{sys}. \tag{13}$$

Where v_c is the asymptotic velocity and v_sys is the systemic velocity. r is defined by the distance to the kinematic centre. r_t is the turnover radius. β is a shape parameter that controls the gradient for $r > r_t$, where the velocity gradient increases for $\beta < 0$, and decreases when $\beta > 0$. γ is a shape parameter that controls how sharply the velocity profile turns over. i is the inclination of the galaxy. Then θ is the polar angle in the plane of the disc.

We intend to estimate the circular velocity from our inferred parameters. While v_c is a natural choice, it is difficult to get a strong constraint on v_c across our complete sample due to the FoV for the SAMI Galaxy Survey typically extending out to ~1.5 R_e. Instead, we estimate the absolute circular velocity at 2.2 R_e denoted as $v_{2.2}$ following (Bloom et al. 2017a).

For low values of i, small differences in the estimated i can result in large difference of $v_{2.2}$. Therefore, for low values of i, incorrect estimates for the observed ellipticity can result in large changes in our estimates for the inclination. As such,

we restrict our calculated values for $v_{2.2}$ to galaxies in the range $i \in [30°, 60°]$ ($e \in [0.13, 0.5]$ assuming a thin disc).

Similarly, galaxies with $R_e < 3.0''$ tended to have very large scatter on their $v_{2.2}$. At these limits, the spatial resolution of our observations are likely playing a role in increasing the scatter in the rotational velocity estimates. 230 galaxies meet the above inclination and R_e criteria. We only reference $v_{2.2}$ for galaxies that meet that inclination for the remainder of this paper.

3.4 Integrated star-formation rates

We used the best fit SFRs from the GAMA Survey (Gunawardhana et al. 2013; Davies et al. 2016; Driver et al. 2018). The SFRs are estimated using full spectral energy distribution (SED) fitting of 21 bands of photometry across the UV, optical, and far infrared ranges with MAGPHYS (da Cunha et al. 2008). MAGPHYS fits the observed photometry using a library that includes stellar spectral and dust emission profiles. In this way, the SFRs are corrected for dust emission. These estimates for the SFR were used instead of the SAMI Hα luminosity maps as there are known aperture affects given the limited FoV of the SAMI instrument (Appendix A, Medling et al. 2018).

For the galaxies from the DYNAMO survey, we used the SFR values reported by Green et al. (2014). SFRs were estimated using the Hα luminosity estimated from their observations. The SFR estimate includes a dust correction using the Balmer decrement from the ratio between their measured Hα and Hβ measurements. The SFR was then calculated using the dust-corrected Hα luminosity maps that were converted to SFR maps using the Kennicutt et al. (1994) conversion assuming a Chabrier (2003) IMF.

3.5 Integrated H I gas measurements

Follow-up 21 cm observations of SAMI galaxies were obtained as part of the SAMI-HI survey, carried out with the Arecibo radio telescope (Catinella et al. in prep.). Observations and data reduction were analogous to those of the xGASS survey (Catinella et al. 2018), with the only difference that these were not gas fraction-limited observations. We observed each galaxy until detected, but moved to another target if there was no hint of H I signal within the first 20-25 minutes of on-source integration.

H I emission-line spectra were obtained for 153 galaxies with these dedicated follow-up observations; on-source integration times ranged between 2 and 50 minutes, with an average of 15 minutes. Together with an additional 143 good HI detections (i.e., classified as detection code '1') in the Arecibo Legacy Fast ALFA (ALFALFA Giovanelli et al. 2005; Haynes et al. 2018) survey, SAMI-H I includes global H I spectra for 296 SAMI galaxies from the SAMI Galaxy Survey catalogue. 95 galaxies overlap with our sample selection from the SAMI Galaxy Survey.

4 RESULTS

4.1 Low gas velocity dispersion in the SAMI Galaxy Survey

We find vertical velocity dispersions lower than previously reported for studies of the gas kinematics in the SAMI Galaxy Survey. The median vertical velocity dispersion is $\sigma_{v,z} = 18.8$ km s^{-1} for our sample as shown in Figure 6. The 68-th shortest credible interval is [14.1, 22.1] km s^{-1} and the 95-th shortest credible interval is [11.4, 30.0] km s^{-1}. The maximum inferred vertical velocity dispersion for a single galaxy is $\sigma_{v,z} = 51$ km s^{-1}. We now compare this to two other studies of the gas kinematics of galaxies from the SAMI Galaxy Survey by Zhou et al. (2017) and Johnson et al. (2018).

Analysing 8 star-forming galaxies in the SAMI Galaxy Survey, Zhou et al. (2017) found that 7 out of 8 galaxies had $\sigma_{gas} \in [20, 31]$ km s^{-1}. Their remaining galaxy (GAMA 508421) was reported as $\sigma_{gas} = 87 \pm 44$ km s^{-1}. GAMA 508421 exhibits a high circular velocity in the outskirts of the SAMI FoV ($v \sim 130$ km s^{-1}) and a clear centralised peak in velocity dispersion that is typical of beam smearing affected galaxies. Our estimate for GAMA 508421 is $\sigma_{v,z} = 22$ km s^{-1}. As such, we suspect that the reported velocity dispersion for GAMA 508421 is greater than it's intrinsic velocity dispersion.

The discrepancy between Zhou et al. (2017) and our estimates, particularly with GAMA 508421, is most likely due to the different beam smearing corrections. Zhou et al. (2017) report the flux-weighted mean velocity dispersion using spaxels where $\sigma_v > 2 v_{grad}$. v_{grad} is an estimate for the local velocity gradient using adjacent spaxels defined as (Varidel et al. 2016),

$$v_{grad}(x, y) = \sqrt{(v(x+1) - v(x-1))^2 + (v(y+1) - v(y-1))^2}. \tag{14}$$

See Section 5.1.1 by Varidel et al. (2019) for a revised calculation of the velocity gradient using a finite-difference scheme.

The approach used by Zhou et al. (2017) usually removes the centre of the galaxies, where the velocity gradient is steepest. This approach results in a significant downward correction compared to the uncorrected velocity dispersion estimates. However, the outskirts of galaxies can still be affected by beam smearing. Also, it is possible that the centre of the galaxy may be effected by beam smearing, yet not reach the $\sigma_v > 2v_{grad}$ criteria, which is likely to have occurred in the case of GAMA 508421. The approach of Zhou et al. (2017) was also shown previously to over-estimate the intrinsic velocity dispersion in toy models (Section 5.1.1., Varidel et al. 2019)

Another study of a sample of 274 star-forming galaxies from the SAMI Galaxy Survey was performed by Johnson et al. (2018). They removed galaxies with $M_* > 8 \times 10^{10}$ M$_\odot$ and Sérsic index of $n > 2$. They also removed galaxies that they deem to be spatially unresolved or have kinematic uncertainties greater than 30%. While they do not provide summary statistics for their inferred velocity dispersion values from the SAMI Galaxy Survey, their plots show a typical range of $\sigma_0 \in [20, 60]$ km s^{-1}, plus one galaxy at $\sigma_0 \sim 90$ km s^{-1}. This is slightly above our range of velocity disperisions.

To estimate the intrinsic velocity dispersion, Johnson et al. (2018) calculated the median velocity dispersion across the kinematic maps or at the outskirts of their galaxy. They then apply a further correction on their estimated velocity dispersion by using a lookup table of toy galaxies that have been constructed with beam smearing effects. The slight difference between our studies may be driven solely by their choice of using a single FWHM estimate for the PSF rather than the Moffat profile used in this paper. Also, increased scatter may occur in their estimator due to being affected by low signal-to-noise spaxels in the outskirts of the galaxies.

4.2 Correlation of global velocity dispersion and integrated star-formation rate

Correlation analysis between the global velocity dispersion and several global galaxy properties from the SAMI Galaxy Survey reveals that $\sigma_{v,z}$ has the greatest positive correlation with star-formation rate measures (Figure 7). We estimate the Spearman-rank correlation between the SFR and $\sigma_{v,z}$ to be $\rho(\text{SFR}, \sigma_{v,z}) = 0.44^{+0.05}_{-0.05}$. We control for several factors in order to investigate this relationship further.

The correlation between $\sigma_{v,z}$ and star-formation rate increases when accounting for the galaxy size. To do this, we estimate the average star-formation rate surface density, $\Sigma_{\text{SFR}} = \text{SFR}/\pi R_e^2$ where R_e is the effective radius. The Spearman-rank correlation is then $\rho(\Sigma_{\text{SFR}}, \sigma_{v,z}) = 0.54^{+0.04}_{-0.04}$. Velocity dispersion is expected to increase with star-formation rate surface density assuming that star-formation feedback processes are acting as a driver of turbulence (e.g. Ostriker & Shetty 2011; Faucher-Giguère et al. 2013). As such, this does provide support that star-formation feedback processes is acting as a driver of turbulence within this sample of galaxies.

Figure 7 also shows a positive correlation between $\sigma_{v,z}$ and integrated stellar mass (M$_*$), H I gas mass (M$_{\text{H I}}$), as well as the sum of M$_*$ and M$_{\text{H I}}$. Interestingly, there is a suggestion that M$_{\text{H I}}$ is slightly more correlated than M$_*$ with $\sigma_{v,z}$, although the uncertainties are wide enough that we cannot confirm that is the case. SFR is well known to be correlated with M$_*$, which adds a further complication in determining the relation between $\sigma_{v,z}$ and SFR.

To account for the SFR $-$ M$_*$ relation, we calculated the specific star-formation rate (sSFR = SFR/M$_*$) and ΔMS. ΔMS is calculated as the log difference between the SFR and the star-forming main sequence relation as proposed by Renzini & Peng (2015). We find that the correlation between $\sigma_{v,z}$ and star-formation rate decreased after accounting for stellar mass. This suggests that the relation between $\sigma_{v,z}$ and star-formation rate is a combination of both SFR and stellar mass related quantities.

Despite the correlation between $\sigma_{v,z}$ and star-formation rate estimators, the absolute change in $\sigma_{v,z}$ as a function of SFR remains slight across the dynamic range of SFR $\in [10^{-3}, 10]$ M$_\odot$ yr^{-1}. We report the change in velocity dispersion in 5 SFR bins in Table 1. The change in mean velocity dispersion between the end bins from SFR = 0.029 M$_\odot$ yr^{-1} to SFR = 2.4 M$_\odot$ yr^{-1} is only 6.41 km s^{-1}. A similarly shallow gradient was found by Johnson et al. (2018) using data from the SAMI Galaxy Survey.

Galaxies are often kinematically classified as either rotationally or turbulence dominated by comparing the ratio of rotational and random velocities (v/σ). In a similar vain to
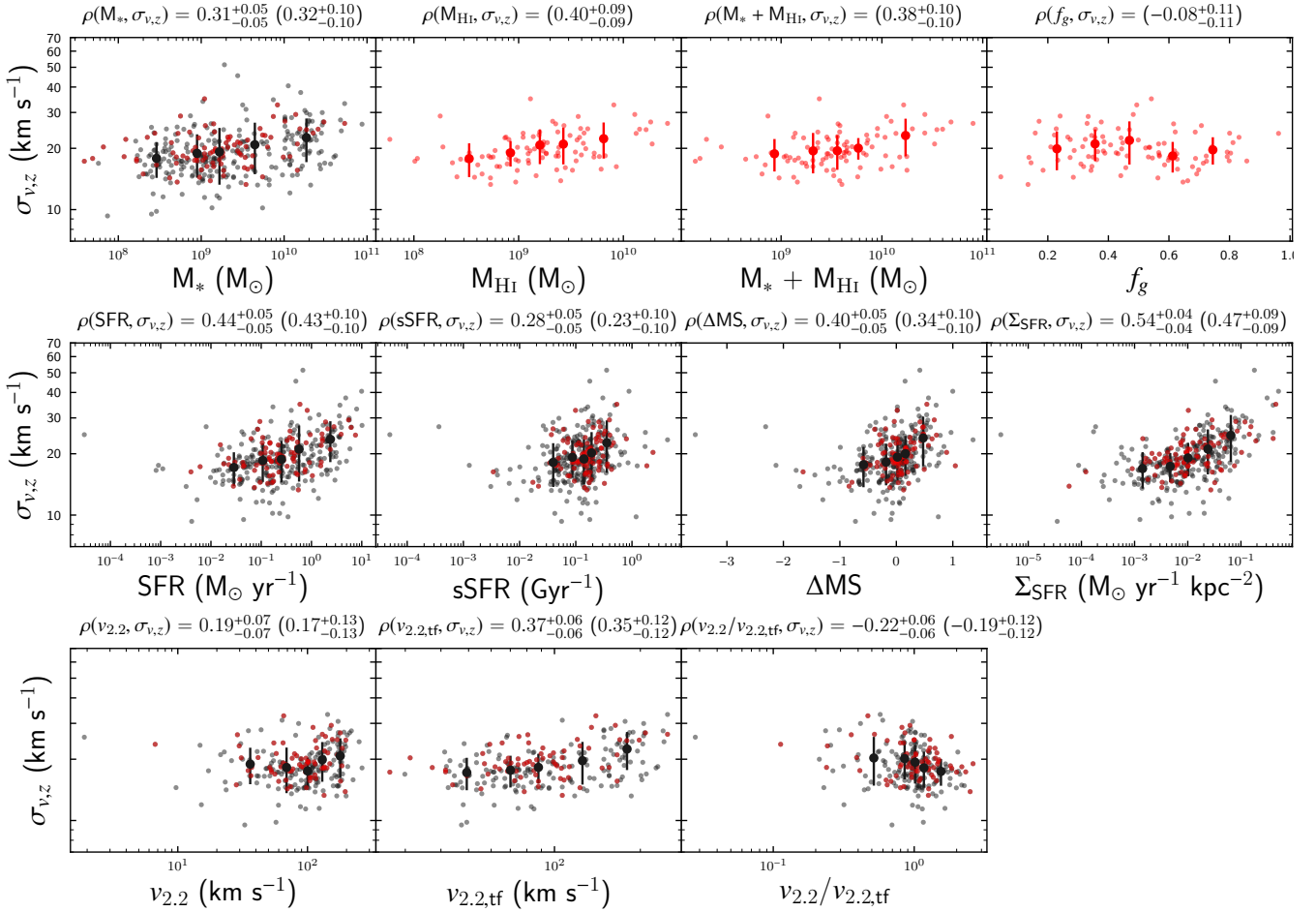
Figure 7. Comparing global intrinsic vertical velocity dispersion ($\sigma_{v,z}$) to global properties for galaxies from the SAMI Galaxy Survey. We show the relation of $\sigma_{v,z}$ with measures of mass (top), star-formation rate (middle), and rotational velocity (bottom), respectively. Red points indicate the galaxies with observed integrated H I masses. The Spearman-rank correlation coefficients are shown at the top of each plot, with brackets indicating the correlation coefficient for galaxies with measured H I masses. The uncertainties for the Spearman-rank correlation coefficients are estimated as the 68% shortest credible interval from 10^4 bootstrapped samples. We find significant positive correlations with measures of mass, star-formation rate, and rotational velocity. The greatest positive correlation we find is with star-formation rate surface density ($\Sigma_{\rm SFR}$).

such analysis, we also investigated the relation between $\sigma_{v,z}$ and rotational velocity. $\sigma_{v,z}$ is shown compared to the rotational velocity measures using BLOBBY3D ($v_{2.2}$) as outlined in Section 3.3 and using the Tully-Fisher relation ($v_{2.2,\rm tf}$, Bloom et al. 2017b).

We find a positive correlation between $\sigma_{v,z}$ and the rotational velocity estimators. This is to be expected as rotational velocity is also correlated with stellar mass. To control for that effect, we calculated the ratio between $v_{2.2}$ and $v_{2.2,\rm tf}$. We then find a negative correlation between $\sigma_{v,z}$ and $v_{2.2}/v_{2.2,\rm tf}$. As such, we observe that galaxies exhibit greater rotation than their mass predicts when $\sigma_{v,z}$ is lesser, and lesser rotation when $\sigma_{v,z}$ is greater.

4.3 Comparisons with other surveys

In this section we aim to describe our results from the SAMI Galaxy Survey in the context of other studies. In Table 1 and Figure 8 we show comparisons of velocity dispersion

compared to SFR. The data is shown in four groups of galaxies; low-z measured using Hα (Epinat et al. 2008; Moiseev et al. 2015), low-z measured using H I (Leroy et al. 2008; Walter et al. 2008; Ianjamasimanana et al. 2012; Stilp et al. 2013), High-z analogues from Varidel et al. (2016) plus the galaxies that we re-analysed from the DYNAMO sample, and high-z galaxies at z $\gtrsim$ 1 (Johnson et al. 2018; Cresci et al. 2009; Wisnioski et al. 2011; Epinat et al. 2009; Law et al. 2009; Jones et al. 2010; Di Teodoro et al. 2016). Table 2 also outlines qualitative ranges for the galaxy parameters for galaxies at low-z measured using the Hα emission line, including other studies of the SAMI and DYNAMO samples.

The comparative data sets have been measured using both ionised and neutral gas. For ionised gas, there are two additional contributions to the velocity dispersion. One is the thermal broadening of $\sigma_{\rm thermal} \sim 9$ km s^{-1}, corresponding to the typical temperature of an H II region. There is also a contribution from the expansion speed of the H II region. Studies of the expansions speed reveal $\sigma_{\rm expand} \sim 10$ km s^{-1}

Table 1. Comparing summary statistics of the vertical velocity dispersion in other samples compared to those in this work. Each sample was split into 5 bins of equal percentile widths. We show the mean ($\bar{\sigma}_{v,z}$), standard deviation ($\Delta\sigma_{v,z}$), the standard error ($\Delta\bar{\sigma}_{v,z}$), median (med($\sigma_{v,z}$)), and bootstrap resampled standard deviation of the median (Δmed($\sigma_{v,z}$)). The groups of galaxies are as follows: Low-z (Hα) (Epinat et al. 2008; Moiseev et al. 2015), H I surveys where 15 km s^{-1} has been added in-quadrature (Leroy et al. 2008; Walter et al. 2008; Ianjamasimanana et al. 2012; Stilp et al. 2013), high-z analogues from Varidel et al. (2016) plus the re-analysed galaxies from the DYNAMO survey, plus high-z (Hα) (Johnson et al. 2018; Cresci et al. 2009; Wisnioski et al. 2011; Epinat et al. 2009; Jones et al. 2010; Di Teodoro et al. 2016).

Group	Bin	SFR (M$_\odot$ yr^{-1})	$\bar{\sigma}_{v,z}$ (km s^{-1})	$\Delta\sigma_{v,z}$ (km s^{-1})	$\Delta\bar{\sigma}_{v,z}$ (km s^{-1})	med($\sigma_{v,z}$) (km s^{-1})	Δmed($\sigma_{v,z}$) (km s^{-1})
SAMI (Hα)	1	0.029	17.12	3.21	0.39	17.13	0.29
	2	0.11	18.54	3.99	0.49	18.31	0.41
	3	0.25	18.79	4.34	0.53	18.52	0.43
	4	0.57	21.07	6.47	0.79	19.72	0.71
	5	2.4	23.54	5.35	0.65	23.54	0.64
Low-z (Hα)	1	0.0047	19.46	2.89	0.43	18.84	0.72
	2	0.046	20.77	4.33	0.65	19.21	0.41
	3	0.18	20.57	3.86	0.58	19.21	0.6
	4	0.37	21.66	4.55	0.68	19.85	0.44
	5	1.0	23.5	7.0	1.0	21.21	0.81
Low-z (H I)	1	0.0014	16.95	0.55	0.18	16.86	0.15
	2	0.005	17.39	0.64	0.20	17.44	0.25
	3	0.066	18.65	2.98	0.99	17.81	0.6
	4	0.58	19.18	1.36	0.43	18.78	0.57
	5	2.2	20.82	2.58	0.82	19.9	1.4
High-z	1	0.96	27.0	3.2	1.1	26.23	0.94
Analogues (Hα)	2	3.2	39.4	12.6	4.4	40.0	4.9
	3	9.1	40.7	14.3	5.0	41.2	7.8
	4	17	43.0	15.2	5.4	42.9	7.6
	5	27	55.9	15.6	5.2	54.8	5.4
High-z (Hα)	1	3.4	44.0	20.5	1.6	39.8	1.9
	2	6.4	45.8	18.2	1.5	43.1	1.2
	3	10	44.3	20.3	1.6	42.8	3.2
	4	20	48.3	20.2	1.6	45.0	1.5
	5	82	53.2	20.0	1.6	51.0	2.6

for small regions, up to $\sigma_{\rm expand} \sim 13 - 17$ km s^{-1} for larger regions (Chu & Kennicutt 1994).

Given the contributions of $\sigma_{\rm thermal}$ and $\sigma_{\rm expand}$ to the observed ionised gas kinematics, we perform several adjustments to the comparative velocity dispersion estimates. For ionised gas estimates, we remove any corrections for the additional contributions. For H I studies, we assume a nominal contribution due to these effects of 15 km s^{-1}, that we add in quadrature to the published velocity dispersion estimates. We note that in other studies, 15 km s^{-1} has been subtracted in quadrature from the ionised gas measurements for comparisons between different studies. We prefer the alternative as 15% of our galaxies have $\sigma_{v,z} < 15$ km s^{-1}.

4.3.1 Comparison with surveys at low-z

The SAMI Galaxy Survey has similar selection criteria to the Mapping Nearby Galaxies at Apache Point Observatory (MaNGA, Bundy et al. 2015) survey in terms of fundamental galaxy properties (see Table 2). Our data have similar ranges in redshifts, stellar mass, and SFR. As such, we would naively expect the gas turbulence within our sample to be similar to the MaNGA survey estimates.

We find systematically lower velocity dispersions than those estimated by Yu et al. (2019). They estimated mean velocity dispersions of $\sigma \in [20, 50]$ km s^{-1} across various galaxy property ranges (Figure 6, Yu et al. 2019). Specifically for SFR vs. velocity dispersion they

found mean $\sigma \in [30, 50]$ km s^{-1} across 4 bins in the range SFR $\in [10^{-2}, 10]$ M$_\odot$ yr^{-1}. Whereas we estimate mean $\bar{\sigma}_{v,z} \in [17, 24]$ km s^{-1} across 5 bins of SFR $\in [10^{-3}, 10]$.

Yu et al. (2019) also reported galaxies with velocity dispersion of $\sigma_v \gtrsim 50$ km s^{-1} up to $\sigma_v \sim 130$ km s^{-1}. This is similar to σ_v estimates for galaxies at high redshift (see high-z galaxies, Table 1). However, we see very little evidence for a significant fraction of galaxies with $\sigma_v \gtrsim 50$ km s^{-1}.

The spectral resolution of $\sigma_{\rm LSF} \in [50, 80]$ km s^{-1} (Bundy et al. 2015; Yu et al. 2019) may be an issue for MaNGA. The variability in the MaNGA spectral resolution could correspond to a large scatter in their estimated velocity dispersion, that may explain their upper limit of $\sigma_v \sim 100$ km s^{-1}. We also show that the velocity dispersion is significantly less than their spectral resolution, thus their assumptions regarding the LSF will be important.

Instead, our results are closer to the velocity dispersion estimates found in the Gassendi HAlpha survey of SPirals (GHASP, Epinat et al. 2008), where their galaxies overlap in SFR. We can see in Figure 8 that our samples match well with the work of Epinat et al. (2008) both in terms of mean velocity dispersion and gradient as a function of SFR. We only disagree slightly in terms of the intrinsic scatter, which could be sample selection, methodology, or signal-to-noise dependent.

We highlight that Epinat et al. (2008) estimated their velocity dispersion using the residuals in spatially resolved mean velocity compared to a rotational velocity model. As
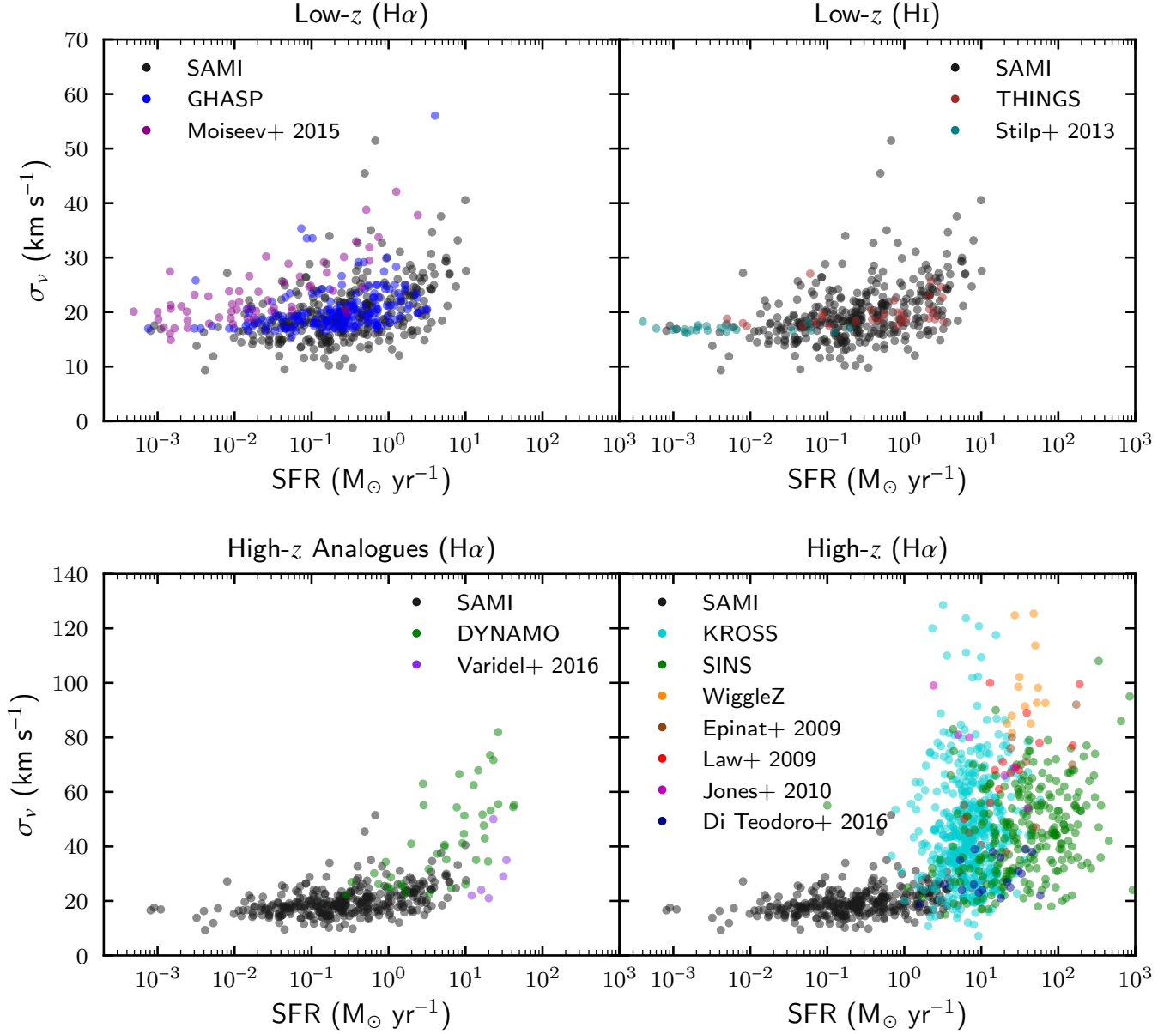
Figure 8. Comparison of the SFR – velocity dispersion (σ_v) relation compared to others surveys in the literature. The sets of galaxies that constitute each subplot are the same as outlined in Table 1. We find the SFR – σ_v relation increases slightly across the range SFR $\in [10^{-3}, 1]$ M$_\odot$ yr^{-1}, then turns up significantly at SFR $\gtrsim 1$ M$_\odot$ yr^{-1}. This relation is approximately consistent across all surveys.

Table 2. Qualitative ranges of galaxy parameters for low-z samples in the literature, where gas kinematics were estimated using the Hα emission line.

Sample	z	$\log_{10}(M_*/M_\odot)$	$\log_{10}(\mathrm{SFR} / M_\odot \ \mathrm{yr}^{-1})$	σ_v (km s^{-1})
SAMI (this work)	[0.005, 0.08]	[7.5, 11]	[-3, 1]	[10, 60]
SAMI (Johnson et al. 2018)	< 0.1	[7.5, 11]	[-3, 1]	[20, 90]
SAMI (Zhou et al. 2017)	< 0.1	[9.8, 10.8]	-	[20, 90]
DYNAMO (this work)	[0.06, 0.15]	[9, 11]	[-1, 2]	[10, 80]
DYNAMO (Green et al. 2014)	[0.06, 0.15]	[9, 11]	[-1, 2]	[10, 90]
GHASP (Epinat et al. 2008)	∼ 0.01	-	[-3, 1]	[15, 30]
Moiseev et al. (2015)	< 90 Mpc	-	[-3, 1]	[15, 40]
Varidel et al. (2016)	[0.01, 0.04]	[10.5, 11]	[1, 1.6]	[20, 50]
MaNGA (Yu et al. 2019)	[0.01, 0.15]	[8.5, 11.5]	[-2, 1]	[10, 130]

such, their measurements are fundamentally different and should not be affected by σ_{thermal} and σ_{expand}. So we added 15 km s^{-1} in quadrature to their published velocity dispersion estimates for comparison purposes.

Our results are also qualitatively similar to those published by Moiseev et al. (2015), who studied a sample of nearby dwarf galaxies. Their results agree with the higher end of our velocity dispersion estimates, although there is still an offset in the mean velocity dispersion. We note that Moiseev et al. (2015) do not explicitly correct for beam smearing, but due to studying nearby galaxies at < 90 Mpc, the effects of beam smearing should be minimal.

Combining the results of Moiseev et al. (2015) and Epinat et al. (2008), we find differences of the mean and median velocity dispersion estimates compared to our sample of $\sim 1 - 3$ km s^{-1} (see Table 1), where our results were systematically lower. The difference of ~ 2 km s^{-1} could be explained due to calculating $\sigma_{v,z}$ rather than $\sigma_{v,\text{LoS}}$, which resulted in a downward shift in our velocity dispersion estimates by ~ 2 km s^{-1} as described in Section 3.2.3.

We find little difference in the intrinsic scatter between our sample and the combined samples of Moiseev et al. (2015) and Epinat et al. (2008). Calculating the 1-sigma standard deviation for the sample ($\Delta\sigma_{v,z}$), sample mean ($\Delta\bar{\sigma}_{v,z}$), and median ($\Delta\text{med}(\sigma_{v,z})$), we find that all variance estimates were of similar magnitude (see Table 1). As such, we conclude that our results are approximately consistent with the analyses of Moiseev et al. (2015) and Epinat et al. (2008) at low-z using ionised gas, albeit with different selection and methodologies in inferring the intrinsic velocity dispersion. The only exception in inferred velocity dispersions at low-z using the ionised gas is the results of Yu et al. (2019) using MaNGA data where we estimate systematically lower σ_v.

Comparisons to the H I observations suggest that we get the same approximately flat SFR $-\sigma_v$ relation across the range SFR $\in [10^{-3}, 10]$ M$_\odot$ yr^{-1}. While there are only slight differences between the mean velocity dispersion of $\sim 1 - 4$ km s^{-1} across varying SFR ranges, it is important to reiterate that the H I results have 15 km s^{-1} added in quadrature, which is the typical difference between H I and Hα estimates for the velocity dispersion. The varying contributions of σ_{thermal} and σ_{expand} may cause a larger scatter than the neutral hydrogen estimates.

4.3.2 *Comparisons with surveys at high-z and high-z analogues*

We now compare our results to those at high-z and high-z analogues. The data sets included are from the DYNAMO survey, which we have re-analysed using Blobby3D. We also include the beam-smearing corrected estimates denoted as $\sigma_{\text{m,uni},v_g=0}$ from Varidel et al. (2016). These samples are of galaxies at low-z with SFR $\gtrsim 1$ M$_\odot$ yr^{-1}, that are similar to galaxies at high-z (see Table 1). As such, high-z analogues are likely to have similar properties to our galaxy sample at similar SFR.

Our re-analysis of the galaxies from the DYNAMO survey find results consistent with Green et al. (2014). The difference between our results and those of Green et al. (2014) are $\sigma_{v,z} - \sigma_{v,\text{green}} = 0.0^{+4.9}_{-6.5}$ km s^{-1}. Follow-up studies of galaxies from the DYNAMO survey have also found similar results

including re-analysis using alternative beam smearing corrections (Bekiaris et al. 2016) and observations using adaptive optics (Oliva-Altamirano et al. 2018).

There is a slight increase in σ_v when comparing SAMI with the high-z analogues at overlapping SFR. At SFR ~ 3 M$_\odot$ yr^{-1}, we estimate $\bar{\sigma}_{v,\text{SAMI}} = 23.54 \pm 0.65$ km s^{-1} compared to $\bar{\sigma}_{v,\text{HzA}} = 27.0 \pm 1.1$ km s^{-1} at SFR ~ 2.4 M$_\odot$ yr^{-1} and $\bar{\sigma}_{v,\text{HzA}} = 39.4 \pm 4.4$ km s^{-1} at SFR ~ 3.2 M$_\odot$ yr^{-1} for the high-z analogues. The highest velocity dispersions are primarily from the DYNAMO survey. We note that while Blobby3D was applied to both samples, the PSF for DYNAMO was assumed to be a Gaussian profile compared to a Moffat profile for the SAMI Galaxy Survey. This may result in an increased beam smearing correction in the SAMI Galaxy Survey compared to the DYNAMO survey. Also, the inclination correction was only applied to SAMI, which resulted in a ~ 2 km s^{-1} subtraction to the initially inferred velocity dispersion from Blobby3D. As such, a difference of ~ 10 km s^{-1} may not be significant given limitations of comparing the two samples.

The high-z analogues extend the trend of increasing σ_v with SFR (see Figure 8). This trend starts to increases within the sample from SAMI Galaxy Survey at SFR $\gtrsim 1$ M$_\odot$ yr^{-1}. Expanding the star-formation rate range up to SFR ~ 100 M$_\odot$ yr^{-1} using the high-z analogues, we see that trend increases dramatically with σ_v up to 80 km s^{-1} in the range SFR $\in [10, 100]$ M$_\odot$ yr^{-1}, which is qualitatively consistent with samples at high-z.

The high-z galaxies exhibit a wide range of $\sigma_v \in [10, 150]$ km s^{-1}. Some of this extent is likely to be driven by lower signal-to-noise at higher redshift. Furthermore, systematic biases such as beam smearing effects, that act to increase σ_v, will be greater due to the lower spatial resolution. Instead, the high-z galaxies still exhibit similar σ_v as the high-z analogues when studied as a group.

The high-z galaxies still exhibit a trend of increasing velocity dispersion as function of SFR. There is a change from $\sigma_v \sim 40$ km s^{-1} to ~ 50 km s^{-1} for SFR of 3 to 82 M$_\odot$ yr^{-1} (see Table 1). We estimated the correlation to be $\rho(\text{SFR}, \sigma_v) = 0.17^{+0.03}_{-0.04}$. This is a weaker correlation between SFR and σ_v than observed in low-z galaxies. Lesser correlation is likely linked to increased scatter for observations of galaxies at high-z. The increase in scatter may be driven by signal-to-noise, beam smearing effects due to lower spatial resolution, or a change in the physical drivers of gas turbulence at high-z.

There is evidence for increased σ_v at high-z compared to the high-z analogues at similar SFRs. In Table 1, we show binned estimators for dynamic ranges of SFR $\in [3, 30]$ M$_\odot$ yr^{-1} for these two samples. σ_v is ~ 5 km s^{-1} higher at similar SFRs for the high-z galaxies compared to the high-z analogues.

5 THE DRIVERS OF TURBULENCE WITHIN LOW-Z GALAXIES

Turbulence in the Interstellar Medium (ISM) is expected to dissipate on the order of the disc crossing time (Mac Low et al. 1998; Stone et al. 1998). Thus, an ongoing energy source is required to maintain supersonic gas turbulence across epochs.

Two proposed drivers are star-formation feedback process and gravity driven turbulence.

5.1 Star formation feedback driven turbulence

Star-formation feedback processes inject momentum into the ISM through several mechanisms. These mechanisms include supernova, stellar winds, expanding H II regions, and radiation pressure from highly dense star clusters. Therefore, there has been a claim that star-formation feedback processes could provide an ongoing source of energy for the supersonic turbulence in the ISM.

Observational studies have routinely found that there is a positive correlation between global σ_v and SFR, that has been used as evidence to support star-formation feedback processes as a driver of turbulence (Green et al. 2010, 2014; Moiseev et al. 2015; Johnson et al. 2018; Übler et al. 2019; Yu et al. 2019). In Section 4.2 we showed that this correlation exists in our sample of galaxies. We also showed that this correlation extends to higher SFR when connecting our sample to other galaxy surveys.

The relationship between SFR and σ_v has also been considered in theoretical and computational studies. Typically, the energy contribution from supernovae is considered to dominate, and therefore, has been the primary focus of most of these studies. The momentum injection per mass of stars is often assumed to be on the order of $\langle p_*/m_* \rangle = 3000$ km s^{-1}. Incorporating this momentum injection into theoretical models results in assuming that the rate of momentum injection is proportional to the star-formation rate surface density, thus $\dot{P} \propto \langle p_*/m_* \rangle \Sigma_{\mathrm{SFR}}$ (e.g. Ostriker & Shetty 2011; Faucher-Giguère et al. 2013; Krumholz et al. 2018). Therefore, we expect the velocity dispersion to be positively correlated with star-formation rate surface density, if star-formation feedback processes is playing a role in driving turbulence in the ISM.

We showed in Section 4.2 that $\sigma_{v,z}$ has a strong positive correlation with the galaxy averaged star-formation rate surface density. This is consistent with other analyses of the star-formation rate density and velocity dispersion (e.g. Lehnert et al. 2009; Yu et al. 2019; Übler et al. 2019). In some cases, this has been used as evidence for star-formation feedback processes acting as a primary driver of turbulence (Lehnert et al. 2009, 2013). Yet if star-formation feedback processes are acting as a driver of turbulence, we should expect that the localised Σ_{SFR} and σ_v are correlated, yet some analyses have found this relation (Lehnert et al. 2009, 2013), and other studies have found a weak or statistically insignificant relation between these localised properties (Genzel et al. 2011; Varidel et al. 2016; Zhou et al. 2017; Übler et al. 2019). Another approach to compare the observed velocity dispersion to the star-formation rate is to construct a bottom-up approach whereby Σ_{SFR} is modeled on the local scale and then integrated across the disc to estimate SFR.

To estimate Σ_{SFR} as a function of galaxy properties, it is first noted that the star-formation rate surface density is a function of the star-forming molecular gas fraction (f_{sf}) of the gas surface density (Σ_{gas}), that is then converted to stars at a star-formation rate efficiency per free-fall time (ϵ_{ff}). Following Krumholz et al. (2018) this can be written as,

$$\Sigma_{\mathrm{SFR}} = \frac{\epsilon_{\mathrm{ff}}}{t_{\mathrm{ff}}} f_{\mathrm{sf}} \Sigma_{\mathrm{gas}}, \tag{15}$$

where the remaining undefined quantity is the free-fall time (t_{ff}). This can then be incorporated into models to make predictions for the velocity dispersion.

One approach is to assume that the star-formation law is retained on the subgalactic scale. This assumes that ϵ_{ff} is approximately constant across the galaxy, which is broadly in agreement with the literature (Krumholz & Tan 2007; Krumholz et al. 2012; Federrath 2013; Salim et al. 2015; Krumholz et al. 2019). While some studies have found evidence for varying ϵ_{ff} as a function of galaxy properties (Hirota et al. 2018; Utomo et al. 2018), the results and implications for the value of ϵ_{ff} remains in dispute. Furthemore, studies using the above approximation have found that $\sigma_{v,z} \lesssim 25$ km s^{-1}, with little variation of $\sigma_{v,z}$ as a function of star-formation rate (Ostriker & Shetty 2011; Krumholz et al. 2018). As noted in the above samples, there is a large population of galaxies with $\sigma_{v,z} \gtrsim 25$ km s^{-1}, particularly at high redshifts. As such, it is unlikely that this model is able to explain the full range of observed $\sigma_{v,z}$. Furthermore, such models allow for the variation of the Toomre Q stability parameter, which leads to disagreements with observations. Hereafter, we will use the 'No Transport, Fixed ϵ_{ff}' model constructed by Krumholz et al. (2018) as representative of such models.

Another approach is to assume that ϵ_{ff} can vary as a function of galaxy properties. One such approach was developed by Faucher-Giguère et al. (2013), which assumes that the Toomre stability criteria Q self-regulates to 1. In their model, when $Q < 1$ the rate of constructing giant molecular clouds (GMCs) increases, thus increasing star-formation efficiency, driving Q upwards to 1. When $Q > 1$ the rate of GMC construction is limited and thus star-formation slows, leading to Q decreasing to 1. The Faucher-Giguère et al. (2013) predicts that ϵ_{ff} increases with molecular gas content of the galaxy, leading to a correlation between SFR and velocity dispersion, thus potentially providing an explanation for the SFR $- \sigma_v$ relation. Hereafter, we will refer to this model as 'No Transport, Fixed Q' and use the analytical model proposed by Krumholz et al. (2018) for comparison in the following sections.

5.2 Gravity driven turbulence

An alternative to star-formation feedback processes is driving of turbulence due to gravitational mechanisms. In such models, the gravitational potential energy of the gas is converted to kinetic energy, thus driving the turbulence in the ISM. Several mechanisms for this to occur are via accretion onto the disc, accretion through the disc, gravitational instabilities in the disc, or gravitational interactions between components of the disc.

During the initial formation of the disc, there is evidence that accretion onto the disc can cause the high levels of gas turbulence. However, this can only be sustained on the order of the accretion time (Aumer et al. 2010; Elmegreen & Burkert 2010). After initial disc formation, the effect of accretion onto the disc is unlikely to have a significant contribution on the gas turbulence (Hopkins et al. 2013).

Instead, it has been shown that the supersonic turbulence initially set in the ISM during galaxy formation will quickly approach a steady-state solution (Krumholz & Burkert 2010). Such a steady state solution can be found where the sole driving force is due to the accretion of gas through the

disc balanced by the loss of turbulence primarily by shocks. This yields prescriptions for radial models of the gas surface density and $\sigma_{v,z}$. Making simplifying assumptions whereby the entire ISM is assumed to be a single star-forming region, and integrating the models over the radial extent of the disc, they derive a relationship that simplifies to SFR $\propto \sigma_{v,z}$, assuming other disc parameters are constant.

The above model is an instantaneous steady state solution, that is a function of the gas accretion rate and energy loss at the time. As the gas accretion rate has decreased over epochs, this model predicts lower gas turbulence in the ISM of galaxies at low-z. In Section 4.3.2 we highlighted that velocity dispersions were ~ 5 km s^{-1} higher in the high-z sample compared to the high-z analogues sample at similar SFR. This is consistent with the velocity dispersion decreasing as a function of decreasing gas accretion rate over time. Numerous other studies have also found that gas turbulence increases as a function of z (Kassin et al. 2012; Wisnioski et al. 2015; Johnson et al. 2018; Übler et al. 2019).

5.3 Combining star-formation feedback and gravity driven turbulence

Krumholz et al. (2018) recently pointed out that star-formation feedback processes can be added as an extra source of energy to the transport equation derived in Krumholz & Burkert (2010). Similar to the previously mentioned models for star-formation feedback processes, they only assume the contribution of supernovae on the gas turbulence.

Their full 'Transport + Feedback' model gives a SFR – $\sigma_{v,z}$ relation of the form,

$$\text{SFR} = \frac{2}{1+\beta} \frac{\phi_a f_{\text{sf}}}{\pi G Q} f_{g,Q} v_c^2 \sigma_{v,z}$$
$$\times \max \left[\sqrt{\frac{2(1+\beta)}{3 f_{g,\text{P}}}} \phi_{\text{mp}} \frac{8 \epsilon_{\text{ff}} f_{g,Q}}{Q}, \frac{t_{\text{orb,out}}}{t_{\text{sf, max}}} \right] \quad (16)$$

f_{sf} is the fraction of the gas in the molecular star-forming phase. $f_{g,P}$ is the fractional contribution of the gas to the self-gravitation pressure at the mid-plane. $f_{g,Q}$ is the fractional gas contribution to the toomre-Q parameter. β describes the slope of the rotation curve ($\beta = d \ln v_c / d \ln r$). $t_{\text{sf, max}}$ corresponds to the maximum star-formation timescale. $t_{\text{orb, out}}$ corresponds to the orbital period at the edge of the star-forming dominated disc. ϕ_a is a constant that accounts for an offset due to observing global rather than local properties, with $\phi_a = 1$ for local galaxies. $\phi_{\text{mp}} = 1.4$ corresponds to the assumed ratio of total pressure compared to turbulent pressure at the mid-plane.

This model results in a SFR – $\sigma_{v,z}$ relation with a floor at 15 km s$^{-1} \lesssim \sigma_{v,z} \lesssim 25$ km s^{-1} (including the expansion and thermal contributions) for the lower SFR region, thus reproducing gas turbulence that is consistent with the 'No Transport, Fixed ϵ_{ff}' model. The SFR – $\sigma_{v,z}$ relation then transitions to SFR $\propto \sigma_{v,z}$ for higher SFR, consistent with the 'No Feedback' model.

Another important contribution of Krumholz et al. (2018) is that after deriving the transport equation, they can use it to find the steady state solutions making various assumptions. The above model assumes that there is a contribution of star-formation driven turbulence ($\sigma_{v,\text{sf}}$) to the

Table 3. Parameter values for Krumholz et al. (2018) theoretical model tracks used for Figure 9.

Parameter	Local dwarf	Local Spiral	High-z
f_{sf}	0.2	0.5	1.0
v_c (km s^{-1})	100	220	200
t_{orb} (Myr)	100	200	200
β	0.5	0.0	0.0
$f_{g,Q} = f_{g,P}$	0.9	0.5	0.7
ϕ_a	1	1	3
SFR$_{\text{min}}$ (M$_\odot$ yr^{-1})	-	-	1
SFR$_{\text{max}}$ (M$_\odot$ yr^{-1})	0.5	50	-

total turbulence ($\sigma_{v,z}$), where

$$\sigma_{v,\text{sf}} = \frac{4 f_{\text{sf}} \epsilon_{\text{ff}} \langle p_*/m_* \rangle}{\sqrt{3 f_{g,P}} \pi \eta \phi_{\text{mp}} \phi_Q \phi_{\text{nt}}^{3/2}}$$
$$\times \max \left[1, \sqrt{\frac{3 f_{g,P}}{8(1+\beta)}} \frac{Q_{\text{min}} \phi_{\text{mp}}}{4 f_{g,Q} \epsilon_{\text{ff}}} \frac{t_{\text{orb}}}{t_{\text{sf, max}}} \right]. \quad (17)$$

Here $\eta = 1.5$ is a scaling parameter for the dissipation rate. $\phi_{\text{mp}} = 1.4$ is the ratio of total to turbulent pressure at the midplane. $\phi_Q = 2$ is the gas to stellar Q plus one. By setting $\sigma_{v,\text{sf}} = 0$, Krumholz et al. (2018) derive the 'No Feedback' model. In that case, the disc must remain stable, such that $Q = 1$.

Krumholz et al. (2018) derive the 'No Transport, Fixed ϵ_{ff}' model by setting $\sigma_{v,z} = \sigma_{v,\text{sf}}$. In that case, the contribution is purely driven by the balance between gravitational collapse and star-formation driven by supernovae outwards. The model is similar to the model proposed by Ostriker & Shetty (2011).

The 'No Transport, Fixed Q' model, is derived by revisiting their transport equation and looking for solutions where Q is set as a constant. They derive a slightly different relation given by,

$$\text{SFR} = \frac{4 \eta \sqrt{\phi_{\text{mp}} \phi_{\text{nt}}^3} \phi_Q}{G Q^2} \left(\frac{p_*}{m_*} \right)^{-1} \frac{f_{g,Q}^2}{f_{g,P}} v_c^2 \sigma_{v,z}^2. \quad (18)$$

The formulation of different drivers using the same theoretical backing allows for a relatively easy comparison between the observations and different model assumptions.

5.4 Comparison with theoretical model tracks

We now compare our observations to the theoretical models described above. We compare our data to the Krumholz et al. (2018) theoretical model tracks for various galaxy groups; low-z dwarfs, low-z spirals, and high-z galaxies. For each galaxy group we use the set of parameters suggested by Krumholz et al. (2018), which are shown in Table 3. To account for the thermal and expansion contributions to the velocity dispersion of the H II regions, 15 km s^{-1} was added in quadrature to the theoretical models.

We find the best agreement between our data and the 'Transport + Feedback' model (Figure 9). The lower-end of the SFR – $\sigma_{v,z}$ relation in the range SFR $\in [10^{-3}, 1]$ M$_\odot$ yr^{-1} is explained by the floor of the 'Transport + Feedback' model tracks, which is driven by star-formation feedback processes. Importantly, the slight increase in $\sigma_{v,z}$ can be explained by a change in galaxy properties across the dynamic range of

SFR. The upturn in the SFR – $\sigma_{v,z}$ relation at SFR $\gtrsim 1$ M$_\odot$ yr^{-1} is also consistent with 'Transport + Feedback' model tracks. This is in contrast to the alternative models, that cannot account for the relation across the full dynamic range of SFR.

The 'No Feedback' model is able to model the upturn in the SFR – $\sigma_{v,z}$ relation, but it cannot account for the lower-end of the relation. At the lower end of the relation, this model assumes $\sigma_{v,z}$ approaches the thermal and expansion contributions alone. We observed that most of our galaxies lie above the assumed $\sigma_{v,z} > 15$ km s^{-1} contributions from the thermal and expansion broadening. Furthermore, there is a positive correlation of $\sigma_{v,z}$ with SFR even at SFR $\lesssim 10$ M$_\odot$ yr^{-1} that the 'No Feedback' model does not appear to account for. Despite the 'No Feedback' model appearing to be a better model, we note that it is difficult to distinguish between the 'No Feedback model' and 'Transport + Feedback' model, as the thermal and expansion broadening contribution is not well known.

The 'No Transport, Fixed $\epsilon_{\rm ff}$' model accounts well for the lower-end SFR – $\sigma_{v,z}$ relation in our sample. However, it predicts very little evolution in $\sigma_{v,z}$ across galaxy properties for low-z galaxies. This is in contrast to the observations that do appear to have an upturn in $\sigma_{v,z}$ for increasing SFR. This suggests that there must be an additional energetic input to the 'No Transport, Fixed $\epsilon_{\rm ff}$' to account for increase $\sigma_{v,z}$ across SFR.

The 'No Transport, Fixed Q' model provides an alternative SFR – $\sigma_{v,z}$ relation (SFR $\propto \sigma_{v,z}^2$). The upturn in the theoretical relation qualitatively matches the observed upturn. However, the model tracks are lower than the observed $\sigma_{v,z}$. Similar to the 'No Feedback' model, increasing the thermal and expansion contributions to $\sigma_{v,z}$ would result in better agreement. The 'No Transport, Fixed Q' cannot account for the increased scatter in $\sigma_{v,z}$ for increasing SFR, due to estimating very little variation in $\sigma_{v,z}$ across most of our dynamic range of SFR.

To distinguish between the 'Transport + Feedback' and 'No Transport, Fixed Q' models, we also compare the theoretical model tracks while varying the circular velocity (see Figure 10). We see generally good agreement between the 'Transport + Feedback' model tracks and the observed velocity dispersion. The upturn in the velocity dispersion occurs approximately at the expected circular velocity.

To quantify the differences, we calculate the relative residuals between the data and the models. To do this, we used the 'local spiral' tracks for SFR < 10 M$_\odot$ yr^{-1} and a model with intermediate parameters between the 'local spiral' and 'high-z' models ($f_{\rm sf} = 0.8$, $t_{\rm orb} = 200$ M$_\odot$ yr^{-1}, $\beta = 0$, $f_{g,Q} = f_{g,P} = 0.6$, $\phi_a = 2$) for SFR ≥ 10 M$_\odot$ yr^{-1}. The relative residuals between the model tracks and data reveal $\Delta\sigma_{v,z}/\sigma_{v,z} = -0.02 \pm 0.32$ for the 'Transport + Feedback' model compared to $\Delta\sigma_{v,z}/\sigma_{v,z} = 0.29 \pm 0.42$ for the 'No Transport, Fixed Q' model. In particular, the relative residuals for the 'No Tranport, Fixed Q' model increase to $\Delta\sigma_{v,z}/\sigma_{v,z} = 1.16 \pm 0.52$ for SFR > 10 M$_\odot$ yr^{-1}. Thus, suggesting that the 'Transport + Feedback' model provides a better fit to the data than the 'No Transport, Fixed Q' model.

For galaxies at SFR $\gtrsim 10$ M$_\odot$ yr^{-1}, we require a transition to values more representative of the high-z galaxy model tracks, with higher $f_{\rm sf}$, $f_{g,Q}$, and $f_{g,P}$ to explain the SFR – $\sigma_{v,z}$ relation. This is not surprising given that those galaxies

were selected from the DYNAMO sample. Many of these galaxies exhibit similar properties to those of high-z galaxies (Green et al. 2014; Fisher et al. 2017) including increased molecular gas fractions (Fisher et al. 2014).

A similar conclusion was reached by Übler et al. (2019), when comparing the 'Transport + Feedback' model tracks as a function of circular velocity for high-z galaxies. They found ~60% of their galaxies could be explained by varying the circular velocity alone.

Increasing the molecular gas fraction ($f_{\rm sf}$) and the gas gravitational contribution at the mid-plane ($f_{g,Q}$, $f_{g,P}$) also shifts the base $\sigma_{v,z}$ by a few km s^{-1}. As galaxies shift to higher $f_{\rm sf}$, $f_{g,Q}$, $f_{g,P}$ as a function of SFR, this provides a mechanism to explain the increase in $\sigma_{v,z}$ seen in the SAMI Galaxy Survey (see Section 3.2.1).

In comparison, the 'No Transport, Fixed Q' model predicts an increase in $\sigma_{v,z}$ as a function of SFR at a slower rate than the 'Transport + Feedback' model. Comparing the model tracks when varying the circular velocity and gas properties, we find that the $\sigma_{v,z} \gtrsim 30$ km s^{-1} are not predicted unless assuming a much lower circular velocity ($v_{2.2,\rm tf} \lesssim 50$ km s^{-1}) than expected given the stellar masses of the galaxies. Increasing the molecular gas content and gas gravitational contribution at the mid-plane as in the high-z galaxies only shifts the model tracks to higher SFR.

The above analysis suggests that the 'Transport + Feedback' model provides a better agreement with the data than those dominated by star-formation feedback processes. This does not completely rule out star-formation feedback processes as the primary driver, instead it may suggest that the assumed energy momentum due to star-formation feedback is too low. The assumed energy source is purely from single supernova, with momentum injection per unit of stars of $\langle p_*/m_* \rangle = 3000$ km s^{-1}. However, $\langle p_*/m_* \rangle$ may be significantly higher if other sources are incorporated. For example, Gentry et al. (2017) argue that $\langle p_*/m_* \rangle$ could be up to an order of magnitude higher when incorporating the effects of clustered supernova. As such, further studies will be required to understand the energetic sources of star-formation feedback processes to incorporate in these models.

As a further caveat to the above analysis, we note that the theoretical models assume that we are observing the star-forming molecular gas, rather than the ionised gas. The full set of differences between the kinematics of the molecular star-forming gas compared to the ionised gas is not complete. For example, there is evidence that ionised gas may have systematically lower rotation and higher velocity dispersions compared to the molecular gas (Levy et al. 2018). However, there is limited research into these differences at this time, as such we make the assumption that these differences are minimal. Further research into the differences in molecular gas and ionised gas kinematics will be required.

5.5 Comparing the correlation analysis to the theoretical models

The above theoretical models (Equations 16 and 18) suggest that SFR $\propto v_c^2$, all else being set equal. Thus, we should expect a strong inverse relationship between $\sigma_{v,z}$ and v_c. In Figure 7 we showed that there is a negative correlation between velocity dispersion and rotational velocity after accounting
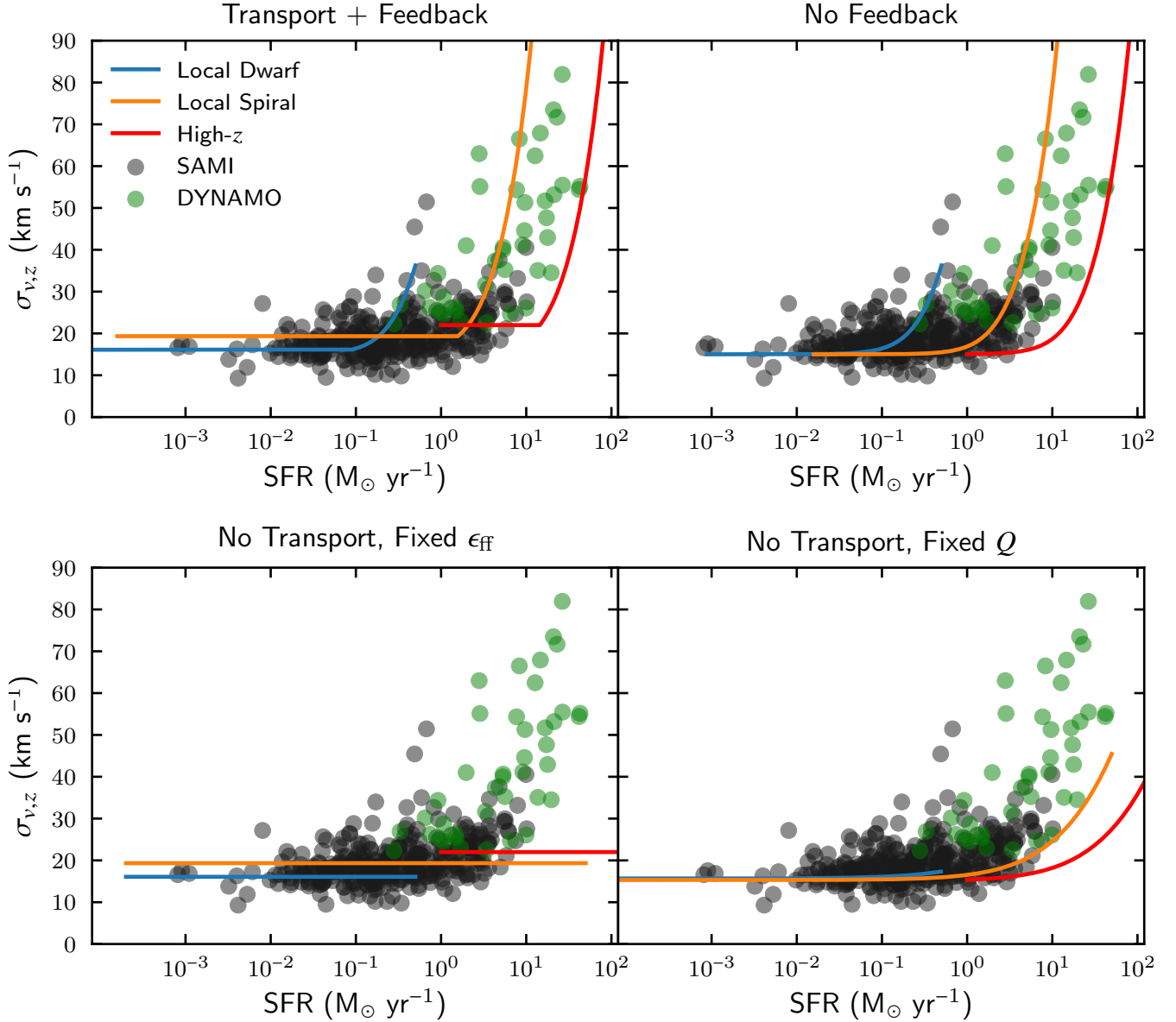
Figure 9. Comparison of the intrinsic vertical velocity dispersion compared to the theoretical model proposed by Krumholz et al. (2018). From left to right, we show the 'Transport + Feedback', 'No Feedback', 'No Transport, Fixed $\epsilon_{\rm ff}$', and 'No Transport, Fixed Q' models. The individual tracks use a set of parameters (see Table 3) that represent typical galaxies for each galaxy type. We find that our observations are the most consistent with the 'Transport + Feedback' model.

for the stellar mass contribution. We are forced to control for the stellar mass using the Tully-Fisher relation as both $\sigma_{v,z}$ and v_c increase for increasing stellar mass.

As such, the rotational velocity is a significant factor in prescribing the intrinsic turbulence within the galaxy. This is consistent with the theoretical models of Krumholz et al. (2018). However, the relationship between the turbulence and rotational velocity does not distinguish between star-formation feedback or gravitational driven mechanisms of turbulence.

The proposed models also suggest a dependence of the SFR – $\sigma_{v,z}$ relation on the mid-plane gas fraction ($f_{g,P}$), the mid-plane gas contribution to the toomre-Q parameter

($f_{g,Q}$), and on the molecular to neutral gas fraction ($f_{\rm sf}$). Krumholz et al. (2018) also showed that galaxy turbulence driven solely by star-formation feedback has the relation SFR $\propto \sigma_v f_{g,Q}^2/f_{g,P}$ whereas solely driven by gravitational mechanisms has SFR $\propto \sigma_v f_{g,Q}^2$.

The contribution of the gas content to the velocity dispersion is difficult to determine in our sample. We have measurements of the integrated H I mass for 95 galaxies in our sample from the SAMI Galaxy Survey. We showed a slight negative but still consistent with zero correlation between the total H I gas fraction (f_g) and $\sigma_{v,z}$ in Section 3.2.1.

A negative correlation between integrated H I mass and $\sigma_{v,z}$ could be due to the expected negative correlation ex-
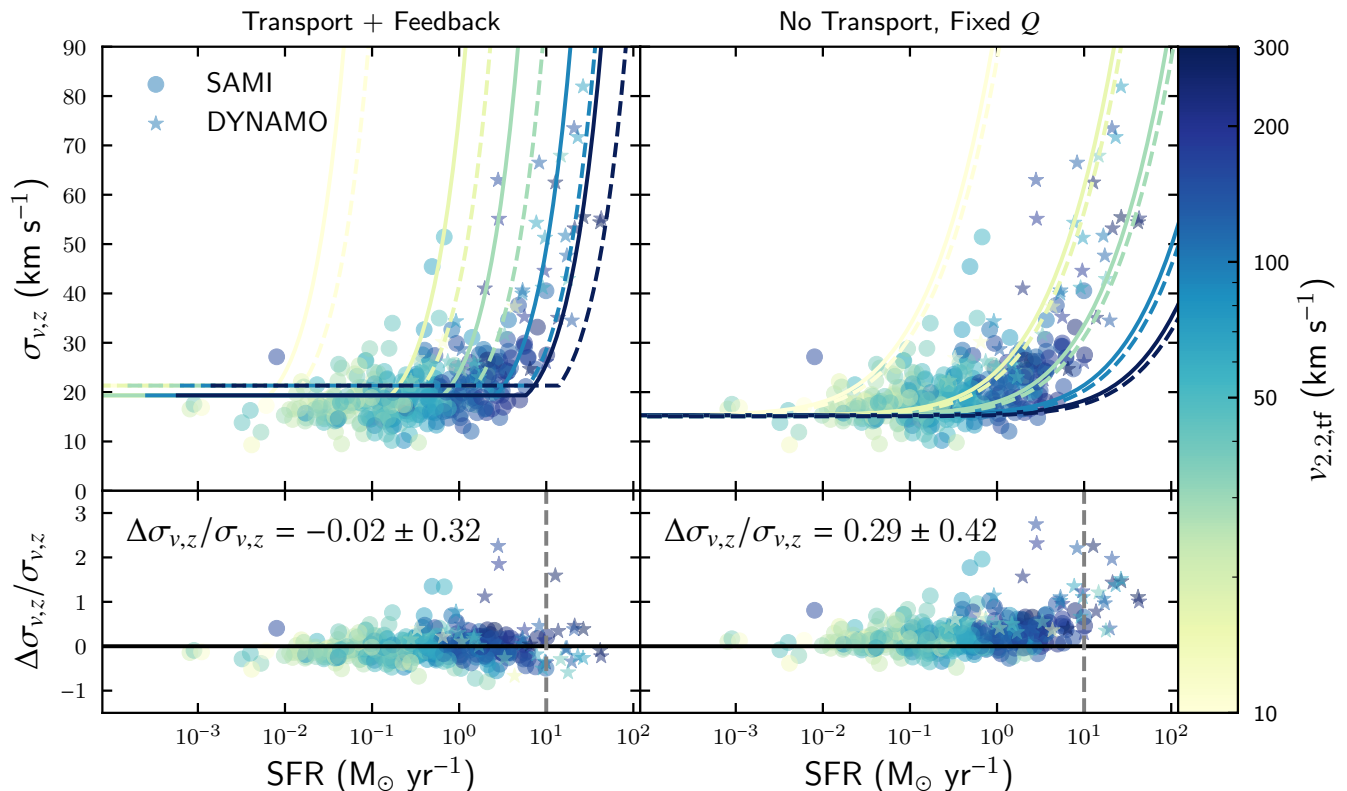
Figure 10. Comparison of the velocity dispersions for the total galaxy sample to the 'Transport + Feedback' (left) and 'No Transport, Fixed Q' (right) models proposed by Krumholz et al. (2018). The top two panels show the data compared to the model tracks, where the data and model tracks are colour coded by $v_{2.2,\mathrm{tf}}$. For all other input parameters to the model tracks, the solid lines use the 'local spiral'. The dashed lines use intermediate values between the 'local spiral' and 'high-z' models; $f_{\mathrm{sf}} = 0.8$, $t_{\mathrm{orb}} = 200$ M$_\odot$ yr^{-1}, $\beta = 0$, $f_{g,Q} = f_{g,P} = 0.6$, $\phi_a = 2$. See Table 3 for the 'local spiral' and 'high-z' parameters. The bottom two panels show the relative residuals, where $\Delta\sigma_{v,z} = \sigma_{v,z} - \sigma_{v,z,\mathrm{model}}$. We use the models represented by the solid lines for SFR < 10 M$_\odot$ yr^{-1} and the dashed lines for SFR $\geq$ 10 M$_\odot$ yr^{-1}. We also show the mean and standard deviation of the relative residuals for each model. Both theoretical models predict an increase in $\sigma_{v,z}$ as a function of SFR, however, 'Transport + Feedback' provides a better fit as a function of circular velocity ($v_{2.2,\mathrm{tf}}$).

pected between $\sigma_{v,z}$ and $f_{g,Q}$ in the 'Transport + Feedback' model. However, it could also be a result of increasing molecular gas fraction (f_{sf}) for increasing SFR and M$_*$ that are also positively correlated with $\sigma_{v,z}$. We also note that the integrated H I measurements are not the ideal measurement as we cannot determine the mid-plane H I gas content within each galaxy. To accurately determine the relation between $\sigma_{v,z}$ and the gas content of the galaxy, we expect that resolved measurements of the H I and H$_2$ masses are required. In that way, we would be able to more precisely determine the mid-plane gravitational contribution of the galaxy gas content. We note that recent work by Sun et al. (2020) has begun to shed light on the mid-plane gas contributions to the observed turbulence, although further studies will be required.

6 CONCLUSIONS

We studied the intrinsic kinematic properties of the ionised gas in 383 low-z star-forming galaxies. 342 galaxies were obtained from the SAMI Galaxy Survey DR2 plus an-

other 41 were from the DYNAMO survey. The total galaxy sample spans a wide range of galaxy properties with SFR $\in [10^{-3}, 10^2]$ M$_\odot$ yr^{-1}. The intrinsic gas kinematics were estimated using BLOBBY3D. BLOBBY3D is a flexible galaxy modelling approach that assumes that the galaxy is regularly rotating with spatially clumpy ionised gas distributions. In order to mitigate the effects of beam smearing and instrumental broadening, a convolution by the PSF and LSF on the underlying model is performed prior to calculating the likelihood function. We also performed a minor inclination correction for the sample from the SAMI Galaxy Survey to estimate the intrinsic vertical velocity dispersion ($\sigma_{v,z}$) as described in Section 3.2.1.

The sample of galaxies from the SAMI Galaxy Survey is a representation of typical galaxies at $z \lesssim 0.1$. As such, we only used that galaxy sample to determine the typical gas kinematics in galaxies at $z \lesssim 0.1$. We find the following:

• Low velocity dispersions of $\sigma_{v,z} \in [14.1, 22.1]$ km s^{-1} for the 68% shortest credible interval. This is ~ 10 km s^{-1} lower than previous studies of the SAMI Galaxy Survey. The difference in results is likely driven by our beam smearing correc-

tion technique using BLOBBY3D, compared to the heuristic approaches applied by Zhou et al. (2017) and Johnson et al. (2018). We also find little evidence for a significant population of galaxies with $\sigma_{v,z} \gtrsim 50$ km s^{-1} as found by Yu et al. (2019) in a sample of galaxies of similar galaxy properties from the MaNGA Survey. In contrast, our velocity dispersions are approximately consistent with other studies of nearby galaxies (Moiseev et al. 2015; Epinat et al. 2008).

• There is a significant positive correlation between $\sigma_{v,z}$ and star-formation rate measures. The greatest correlation was with Σ_{SFR}. Although, the correlation is significant, the average $\sigma_{v,z}$ only increased by ~ 6 km s^{-1} for a dynamic range of SFR $\in [10^{-3}, 10]$ M$_\odot$ yr^{-1}.

• We also find positive correlations of $\sigma_{v,z}$ with integrated stellar and H I gas mass as well as absolute rotational velocity.

• After controlling for stellar mass, there is a negative correlation between $\sigma_{v,z}$ and rotational velocity. This is consistent with theoretical models proposed by Krumholz et al. (2018) for both star-formation feedback processes and gravitational driving mechanisms of turbulence.

• We find a weak, but still consistent with zero, negative trend between $\sigma_{v,z}$ and the integrated H I gas fraction. Theoretical models have suggested that there should be a relation between the gravitational contributions of the gas at the mid-plane and $\sigma_{v,z}$. We suspect that the signal between gas fraction and $\sigma_{v,z}$ is lost when using the integrated H I mass. Accurately determining the gravitational contributions of both H I and H$_2$ at the mid-plane is likely required to observe the proposed relations.

The combined SAMI Galaxy Survey and DYNAMO data sets span a wide range of SFR, allowing for improved comparisons to the theoretical models proposed by Krumholz et al. (2018). The SFR $– \sigma_{v,z}$ relation for our sample of galaxies is the most consistent with the 'Transport + Feedback' model proposed by Krumholz et al. (2018). We find that the SFR $– \sigma_{v,z}$ relation can be approximately explained by a transition of increasing circular velocity and molecular gas at higher SFR.

ACKNOWLEDGEMENTS

REFERENCES

Aumer M., Burkert A., Johansson P. H., Genzel R., 2010, ApJ, 719, 1230
Bekiaris G., Glazebrook K., Fluke C. J., Abraham R., 2016, MNRAS, 455, 754
Bland-Hawthorn J., et al., 2011, Optics Express, 19, 2649
Bloom J. V., et al., 2017a, MNRAS, 465, 123
Bloom J. V., et al., 2017b, MNRAS, 472, 1809
Brewer B., Foreman-Mackey D., 2018, Journal of Statistical Software, Articles, 86, 1
Brewer B. J., Pártay L. B., Csányi G., 2011, Statistics and Computing, 21, 649
Bryant J. J., Bland-Hawthorn J., Fogarty L. M. R., Lawrence J. S., Croom S. M., 2014, MNRAS, 438, 869
Bryant J. J., et al., 2015, MNRAS, 447, 2857
Bundy K., et al., 2015, ApJ, 798, 7
Cappellari M., 2019, arXiv e-prints, p. arXiv:1907.09894
Catinella B., et al., 2018, MNRAS, 476, 875
Ceverino D., Dekel A., Bournaud F., 2010, MNRAS, 404, 2151
Chabrier G., 2003, PASP, 115, 763
Chu Y.-H., Kennicutt Robert C. J., 1994, ApJ, 425, 720
Cid Fernandes R., Stasińska G., Mateus A., Vale Asari N., 2011, MNRAS, 413, 1687
Courteau S., 1997, AJ, 114, 2402
Cresci G., et al., 2009, ApJ, 697, 115
Croom S. M., et al., 2012, MNRAS, 421, 872
Davies R., et al., 2011, ApJ, 741, 69
Davies L. J. M., et al., 2016, MNRAS, 461, 458
Dekel A., et al., 2009, Nature, 457, 451
Di Teodoro E. M., Fraternali F., 2015, MNRAS, 451, 3021
Di Teodoro E. M., Fraternali F., Miller S. H., 2016, A&A, 594, A77
Dobbs C. L., Bonnell I. A., 2007, MNRAS, 374, 1115
Dopita M., Hart J., McGregor P., Oates P., Bloxham G., Jones D., 2007, Ap&SS, 310, 255
Driver S. P., et al., 2011, MNRAS, 413, 971
Driver S. P., et al., 2018, MNRAS, 475, 2891
Elmegreen B. G., Burkert A., 2010, The Astrophysical Journal, 712, 294
Epinat B., Amram P., Marcelin M., 2008, MNRAS, 390, 466
Epinat B., et al., 2009, A&A, 504, 789
Epinat B., Amram P., Balkowski C., Marcelin M., 2010, MNRAS, 401, 2113

Faucher-Giguère C.-A., Quataert E., Hopkins P. F., 2013, MNRAS, 433, 1970

Federrath C., 2013, MNRAS, 436, 3167

Federrath C., et al., 2016, ApJ, 832, 143

Federrath C., et al., 2017, in Crocker R. M., Longmore S. N., Bicknell G. V., eds, IAU Symposium Vol. 322, The Multi-Messenger Astrophysics of the Galactic Centre. pp 123–128 (arXiv:1609.08726), doi:10.1017/S1743921316012357

Fisher D. B., et al., 2014, ApJ, 790, L30

Fisher D. B., et al., 2017, MNRAS, 464, 491

Foreman-Mackey D., 2016, The Journal of Open Source Software, 1, 24

Foreman-Mackey D., Hogg D. W., Lang D., Goodman J., 2013, PASP, 125, 306

Förster Schreiber N. M., et al., 2009, ApJ, 706, 1364

Gentry E. S., Krumholz M. R., Dekel A., Madau P., 2017, MNRAS, 465, 2471

Genzel R., et al., 2006, Nature, 442, 786

Genzel R., et al., 2011, ApJ, 733, 101

Giovanelli R., et al., 2005, AJ, 130, 2613

Glazebrook K., 2013, Publications of the Astronomical Society of Australia, 30, e056

Green A. W., et al., 2010, Nature, 467, 684

Green A. W., et al., 2014, MNRAS, 437, 1070

Green A. W., et al., 2018, MNRAS, 475, 716

Gunawardhana M. L. P., et al., 2013, MNRAS, 433, 2764

Haynes M. P., et al., 2018, ApJ, 861, 49

Hinshaw G., et al., 2009, ApJS, 180, 225

Hirota A., et al., 2018, PASJ, 70, 73

Hopkins P. F., Kereš D., Murray N., 2013, Monthly Notices of the Royal Astronomical Society, 432, 2639

Ianjamasimanana R., de Blok W. J. G., Walter F., Heald G. H., 2012, AJ, 144, 96

Johnson H. L., et al., 2018, MNRAS, 474, 5076

Jones T. A., Swinbank A. M., Ellis R. S., Richard J., Stark D. P., 2010, MNRAS, 404, 1247

Kassin S. A., et al., 2012, The Astrophysical Journal, 758, 106

Kauffmann G., et al., 2003, MNRAS, 346, 1055

Kelvin L. S., et al., 2012, MNRAS, 421, 1007

Kennicutt Robert C. J., Tamblyn P., Congdon C. E., 1994, ApJ, 435, 22

Krumholz M., Burkert A., 2010, ApJ, 724, 895

Krumholz M. R., Burkhart B., 2016, MNRAS, 458, 1671

Krumholz M. R., Matzner C. D., 2009, ApJ, 703, 1352

Krumholz M. R., Tan J. C., 2007, ApJ, 654, 304

Krumholz M. R., Dekel A., McKee C. F., 2012, ApJ, 745, 69

Krumholz M. R., Burkhart B., Forbes J. C., Crocker R. M., 2018, MNRAS, 477, 2716

Krumholz M. R., McKee C. F., Bland -Hawthorn J., 2019, ARA&A, 57, 227

Law D. R., Steidel C. C., Erb D. K., Larkin J. E., Pettini M., Shapley A. E., Wright S. A., 2007, ApJ, 669, 929

Law D. R., Steidel C. C., Erb D. K., Larkin J. E., Pettini M., Shapley A. E., Wright S. A., 2009, ApJ, 697, 2057

Lehnert M. D., Nesvadba N. P. H., Le Tiran L., Di Matteo P., van Driel W., Douglas L. S., Chemin L., Bournaud F., 2009, ApJ, 699, 1660

Lehnert M. D., Le Tiran L., Nesvadba N. P. H., van Driel W., Boulanger F., Di Matteo P., 2013, A&A, 555, A72

Lemoine-Busserolle M., Bunker A., Lamareille F., Kissler-Patig M., 2010, MNRAS, 401, 1657

Leroy A. K., Walter F., Brinks E., Bigiel F., de Blok W. J. G., Madore B., Thornley M. D., 2008, AJ, 136, 2782

Levy R. C., et al., 2018, ApJ, 860, 92

Mac Low M.-M., 1999, ApJ, 524, 169

Mac Low M.-M., Klessen R. S., 2004, Reviews of Modern Physics, 76, 125

Mac Low M.-M., Klessen R. S., Burkert A., Smith M. D., 1998, Phys. Rev. Lett., 80, 2754

Matzner C. D., 2002, ApJ, 566, 302

Medling A. M., et al., 2018, MNRAS, 475, 5194

Moiseev A. V., Tikhonov A. V., Klypin A., 2015, MNRAS, 449, 3568

Murray N., Quataert E., Thompson T. A., 2010, ApJ, 709, 191

Norman C. A., Ferrara A., 1996, ApJ, 467, 280

Oliva-Altamirano P., Fisher D. B., Glazebrook K., Wisnioski E., Bekiaris G., Bassett R., Obreschkow D., Abraham R., 2018, MNRAS, 474, 522

Ostriker E. C., Shetty R., 2011, ApJ, 731, 41

Owers M. S., et al., 2019, ApJ, 873, 52

Renzini A., Peng Y.-j., 2015, ApJ, 801, L29

Salim D. M., Federrath C., Kewley L. J., 2015, ApJ, 806, L36

Scott N., et al., 2018, MNRAS, 481, 2299

Sharp R., et al., 2006, in Society of Photo-Optical Instrumentation Engineers (SPIE) Conference Series. p. 62690G (arXiv:astro-ph/0606137), doi:10.1117/12.671022

Sharp R., et al., 2015, MNRAS, 446, 1551

Skilling J., 2004, in Fischer R., Preuss R., Toussaint U. V., eds, American Institute of Physics Conference Series Vol. 735, American Institute of Physics Conference Series. pp 395–405, doi:10.1063/1.1835238

Stilp A. M., Dalcanton J. J., Skillman E., Warren S. R., Ott J., Koribalski B., 2013, ApJ, 773, 88

Stone J. M., Ostriker E. C., Gammie C. F., 1998, ApJ, 508, L99

Sun J., et al., 2020, ApJ, 892, 148

Taylor E. N., et al., 2011, MNRAS, 418, 1587

Toomre A., 1964, ApJ, 139, 1217

Übler H., et al., 2019, ApJ, 880, 48

Utomo D., et al., 2018, ApJ, 861, L18

Varidel M., Pracy M., Croom S., Owers M. S., Sadler E., 2016, Publ. Astron. Soc. Australia, 33, e006

Varidel M. R., et al., 2019, MNRAS, p. 659

Walter F., Brinks E., de Blok W. J. G., Bigiel F., Kennicutt Robert C. J., Thornley M. D., Leroy A., 2008, AJ, 136, 2563

Wisnioski E., et al., 2011, MNRAS, 417, 2601

Wisnioski E., et al., 2015, ApJ, 799, 209

York D. G., et al., 2000, AJ, 120, 1579

Yu X., et al., 2019, MNRAS, 486, 4463

Zhou L., et al., 2017, MNRAS, 470, 4573

da Cunha E., Charlot S., Elbaz D., 2008, MNRAS, 388, 1595

van de Sande J., et al., 2017, ApJ, 835, 104

APPENDIX A: GALAXY SAMPLE PROPERTIES

Table A1: Galaxy properties for the sample from the SAMI Galaxy Survey analysed in this work. We present the (*a*) spectroscopic redshift (z_spec, Driver et al. 2011; Bryant et al. 2015), (*b*) the stellar mass (M_*, Taylor et al. 2011; Bryant et al. 2015), (*c*) effective radius (R_e, Taylor et al. 2011; Bryant et al. 2015), (*d*) photometric ellipticity ($e = 1 - b/a$, Kelvin et al. 2012; Bryant et al. 2015), and (*e*) SFR (Gunawardhana et al. 2013; Davies et al. 2016; Driver et al. 2018) from the GAMA Survey. We also show the (f) Tully-Fisher circular velocity at $r = 2.2R_e$ calculated using the relationship proposed by Bloom et al. ($v_{2.2,\text{tf}}$, 2017b). The BLOBBY3D inferred (*f*) circular velocity at $r = 2.2R_e$ ($v_{2.2}$) and (*g*) the LoS velocity dispersion ($\sigma_{v,\text{LoS}}$). We also report the (*h*) vertical velocity dispersion ($\sigma_{v,z}$) using the inclination correction outlined in Section 3.2.1.

GAMA ID	RA	Dec	z_spec^a	$\log_{10}(M_*)^b$	R_e^c	e^d	$\log_{10}(\text{SFR})^e$	$v_{2.2,\text{tf}}^f$	$v_{2.2}^g$	$\sigma_{v,\text{LoS}}^h$	$\sigma_{v,z}^i$
	(°)	(°)		($M_\odot$)	(kpc)		($M_\odot \text{ yr}^{-1}$)	(km s^{-1})	(km s^{-1})	(km s^{-1})	(km s^{-1})
8353	182.01649	0.69761	0.020	9.44	2.43	0.37	-0.35	99	112	22	19
8562	182.79067	0.78576	0.020	8.42	2.09	0.28	-1.4	48	15	13	12
8570	182.83286	0.80475	0.021	9.27	2.27	0.35	-0.84	88	60	18	16
8913	184.22040	0.76587	0.029	8.79	1.78	0.45	-4.5	62	-	29	25
9163	185.14066	0.78806	0.007	9.22	2.01	0.45	-1.1	85	35	21	18
9352	185.97719	0.83053	0.024	8.97	1.12	0.47	-0.83	71	-	27	23
14555	212.11498	0.70029	0.026	8.92	2.54	0.46	0.18	68	72	21	17
14812	212.93002	0.72011	0.025	9.99	2.72	0.24	-0.04	147	141	20	18
15218	214.59860	0.73213	0.026	9.11	5.22	0.45	-0.68	78	115	22	19
16948	221.10413	0.78286	0.026	8.89	2.98	0.17	-0.57	67	120	17	16
22932	179.63289	1.13192	0.039	9.47	4.06	0.02	-0.28	101	-	21	21
23337	181.22757	1.21561	0.021	9.74	3.02	0.30	-1.0	123	98	16	14
24414	185.53729	1.11275	0.023	8.35	2.52	0.30	-1.6	46	99	17	15
28654	211.81607	1.06503	0.035	9.14	2.38	0.20	-0.56	80	102	21	19
28738	213.15055	1.05790	0.046	10.05	2.60	0.42	0.077	153	-	27	23
30346	174.63865	-1.18449	0.021	10.45	5.33	0.32	0.43	204	184	22	19
30377	174.82286	-1.07931	0.027	8.22	2.29	0.35	-1.4	42	96	20	17
30890	177.25796	-1.10260	0.020	9.79	3.45	0.43	-0.28	127	123	25	22
32249	183.95869	-1.23808	0.021	8.51	2.72	0.12	-1.2	51	-	18	17
32274	184.15297	-1.08234	0.021	8.79	2.18	0.41	-0.89	62	74	19	16
32362	184.53565	-1.06411	0.019	10.41	6.02	0.44	-0.024	198	197	29	25
37050	215.90251	-1.06030	0.031	9.12	3.75	0.30	-0.7	79	100	19	17
39108	175.13410	-0.66962	0.027	8.35	1.63	0.17	-0.98	46	-	25	23
39145	175.43607	-0.68800	0.050	10.20	2.22	0.24	0.68	171	-	42	38
40283	180.46207	-0.65541	0.019	8.90	3.62	0.23	-1.8	67	50	16	15
40420	181.10961	-0.63196	0.020	9.21	3.62	0.36	-1.6	84	108	25	22
40765	182.89697	-0.69958	0.035	9.04	0.64	0.41	-0.23	75	-	41	35
40916	183.54716	-0.83157	0.025	9.82	6.33	0.45	-0.07	130	128	22	19
41173	184.54418	-0.74498	0.021	8.39	2.25	0.41	-1.4	47	23	18	15
47224	211.86055	-0.74540	0.035	9.16	1.14	0.40	-0.59	81	-	19	17
47500	213.25280	-0.83100	0.026	9.49	1.66	0.46	-0.25	103	-	26	22
47652	213.60344	-0.82934	0.040	9.43	2.64	0.14	0.00043	98	61	21	19
49730	222.29648	-0.70189	0.043	9.51	2.31	0.01	-0.29	104	-	22	22
49753	222.49249	-0.63135	0.026	8.76	3.27	0.40	-1.5	61	90	18	16
49755	222.38983	-0.78424	0.027	8.55	1.46	0.34	-0.92	53	-	20	18
49840	222.72006	-0.67251	0.042	9.22	4.17	0.31	-0.57	85	97	13	11
53809	175.11901	-0.39364	0.027	9.05	1.74	0.44	-0.64	75	-	21	18
53977	176.01840	-0.21097	0.048	10.01	4.04	0.20	0.43	149	122	28	26
54102	176.75303	-0.29422	0.005	8.89	1.21	0.48	-1.5	67	76	17	15
54359	177.74299	-0.36795	0.043	10.30	4.90	0.13	0.18	183	-	20	19
54382	177.89815	-0.37489	0.019	8.54	1.02	0.44	-1.2	52	-	23	19
54455	178.22625	-0.23571	0.026	9.13	5.43	0.49	-0.4	79	36	20	17
55160	180.63455	-0.38942	0.022	8.43	2.45	0.38	-0.93	48	31	28	24
55227	180.94630	-0.33660	0.020	8.33	3.04	0.33	-1.4	45	80	17	15
55346	181.69378	-0.27375	0.034	9.10	2.70	0.45	-0.76	78	68	17	15
55367	181.79334	-0.25959	0.022	8.40	3.36	0.30	-1.4	47	33	11	10
55648	183.00180	-0.37212	0.035	8.97	2.06	0.41	-0.68	71	-	16	14
56061	184.42641	-0.22620	0.041	9.13	2.22	0.31	-1.0	79	-	17	15
62435	212.84807	-0.30051	0.026	9.00	1.68	0.18	-0.95	72	-	20	19

GAMA ID	RA (°)	Dec (°)	$z_{\rm spec}^a$	$\log_{10}({\rm M}_*)^b$ (M$_\odot$)	R_e^c (kpc)	e^d	$\log_{10}({\rm SFR})^e$ (M$_\odot$ yr^{-1})	$v_{2.2,{\rm tf}}^f$ (km s^{-1})	$v_{2.2}^g$ (km s^{-1})	$\sigma_{v,{\rm LoS}}^h$ (km s^{-1})	$\sigma_{v,z}^i$ (km s^{-1})
63210	215.01946	-0.31480	0.051	10.30	2.91	0.43	-0.28	183	-	32	27
63389	215.75063	-0.25454	0.055	10.07	5.45	0.42	0.31	155	162	20	17
63855	217.29079	-0.35168	0.035	9.56	5.16	0.13	0.37	108	-	21	20
64087	218.09196	-0.22671	0.055	10.37	3.39	0.49	0.33	193	-	27	23
65237	222.08657	-0.32651	0.044	9.15	5.22	0.30	-0.59	81	132	20	18
69620	175.72473	0.16189	0.018	9.30	1.91	0.25	-0.24	90	79	24	21
69653	175.85485	0.01404	0.018	8.64	2.84	0.40	-0.91	56	57	25	21
71099	183.06138	0.07230	0.008	8.46	0.74	0.23	-1.1	49	37	18	17
71146	183.25125	0.04376	0.021	9.15	4.04	0.32	-0.6	81	94	21	18
71269	183.97349	0.08162	0.041	9.09	2.32	0.48	0.02	77	-	21	18
71382	184.62741	0.01323	0.021	8.95	1.90	0.19	-1.0	70	129	20	18
77373	212.98003	0.07655	0.040	9.00	4.76	0.50	-0.77	72	104	19	16
77446	213.26064	0.14638	0.055	10.33	5.85	0.16	0.36	187	157	26	24
77754	214.64775	0.15772	0.053	10.48	8.20	0.44	0.79	208	179	32	27
78406	216.98714	0.02259	0.024	8.99	3.09	0.15	-0.86	72	111	19	17
78425	217.06865	0.00231	0.053	10.05	2.49	0.36	1.0	153	-	47	41
78667	218.09082	0.17812	0.055	10.16	8.25	0.22	0.37	166	170	23	21
78921	219.16095	0.11740	0.030	9.44	5.78	0.45	-0.43	99	112	19	16
79601	222.34769	0.04231	0.044	9.05	2.21	0.09	-0.27	75	-	18	17
79710	222.74198	0.09219	0.042	9.18	2.78	0.40	-1.1	82	54	21	18
79712	222.80757	0.02796	0.023	8.57	0.99	0.28	-1.4	53	-	25	22
84048	175.78879	0.55890	0.019	8.66	2.10	0.33	-1.6	57	149	22	19
84107	175.99843	0.42801	0.029	9.71	3.21	0.23	0.21	120	155	28	25
85481	182.70962	0.59591	0.020	9.02	1.99	0.41	-2.5	73	114	16	14
86116	185.27934	0.46134	0.007	7.69	0.51	0.38	-1.7	28	-	21	18
91627	212.81851	0.48944	0.053	10.31	7.86	0.29	0.49	185	179	22	19
99511	183.12848	0.89422	0.021	8.71	2.68	0.13	-1.1	59	-	15	14
99513	183.15825	0.89339	0.020	8.42	2.19	0.10	-1.9	48	-	17	16
99795	184.23281	0.91977	0.029	8.95	2.11	0.05	-0.48	70	-	18	17
100162	185.79312	0.93489	0.026	9.15	1.57	0.50	-0.65	81	-	19	16
100192	185.92766	0.96219	0.024	9.33	3.04	0.08	-0.66	92	-	23	22
105573	212.54694	0.86584	0.026	8.54	1.14	0.39	-1.1	52	-	13	12
105962	214.14784	0.88664	0.026	8.96	3.37	0.36	-0.84	70	65	22	19
106042	214.56214	0.89109	0.026	10.14	7.81	0.20	0.74	163	152	32	29
106331	215.51320	0.86205	0.036	9.61	5.54	0.44	-0.13	112	107	19	16
106376	215.81121	0.97834	0.040	10.27	7.46	0.15	0.88	179	115	26	25
106717	217.01889	1.00631	0.026	10.19	2.93	0.30	0.59	169	170	28	25
107594	221.07590	0.85401	0.026	8.93	3.53	0.47	-0.67	69	115	22	19
136917	176.35594	-1.73764	0.029	9.11	1.87	0.42	-0.87	78	-	18	16
136980	176.53583	-1.82683	0.027	8.63	4.07	0.44	-1.1	56	75	16	14
137071	177.07578	-1.64035	0.013	8.71	0.84	0.20	-0.052	59	-	28	25
137155	177.21879	-1.84390	0.028	8.39	3.61	0.22	-1.5	47	62	21	19
137789	179.57125	-1.72809	0.019	8.57	1.57	0.30	-1.2	53	64	22	19
137847	179.79836	-1.70706	0.020	9.16	2.63	0.33	-0.49	81	46	25	22
138066	180.72149	-1.77911	0.035	9.85	4.29	0.41	-0.61	133	102	19	16
138094	180.74242	-1.70226	0.021	8.77	2.24	0.32	-2.3	61	60	14	12
144197	179.32270	-1.37420	0.026	9.13	1.08	0.21	-0.61	79	-	26	24
144236	179.35020	-1.31321	0.026	8.61	0.99	0.45	-0.93	55	-	23	20
144320	179.73348	-1.43043	0.052	10.27	1.96	0.30	-0.03	179	-	34	30
144402	179.96120	-1.38195	0.036	10.25	3.25	0.35	0.55	177	172	35	31
144497	180.37719	-1.43612	0.035	9.28	1.09	0.12	-0.17	88	-	55	51
144682	181.03465	-1.41719	0.035	9.02	1.03	0.41	-0.77	73	-	40	34
145267	183.70061	-1.34594	0.032	9.12	1.37	0.47	-1.1	79	-	31	26
145583	185.32451	-1.25413	0.022	9.39	3.61	0.41	-0.8	96	85	17	14
176955	174.94289	-1.87526	0.058	10.62	9.09	0.34	0.7	230	204	21	18
177081	175.53937	-1.90905	0.020	8.92	1.47	0.33	-0.34	68	81	30	26
177481	176.91006	-1.92285	0.027	8.84	1.61	0.30	-1.4	65	-	22	19
178481	180.44250	-1.93475	0.025	9.00	4.51	0.29	-0.72	72	109	20	18
178580	180.81309	-1.95678	0.021	8.43	1.75	0.00	-1.4	48	-	20	20

| GAMA ID | RA | Dec | $z_{\rm spec}^a$ | $\log_{10}(M_*)^b$ | R_e^c | e^d | $\log_{10}({\rm SFR})^e$ | $v_{2.2,\rm tf}^f$ | $v_{2.2}^g$ | $\sigma_{v,\rm LoS}^h$ | $\sigma_{v,z}^i$ |
	(°)	(°)		(M⊙)	(kpc)		(M⊙ yr^{-1})	(km s^{-1})	(km s^{-1})	(km s^{-1})	(km s^{-1})
183932	174.27021	-1.60977	0.022	8.27	1.86	0.16	-1.2	43	26	21	20
184234	175.68429	-1.48754	0.029	9.01	4.37	0.05	-0.62	73	-	21	21
184370	176.21728	-1.53212	0.026	9.65	2.55	0.14	-0.56	115	36	20	19
184415	176.34198	-1.56521	0.028	9.56	2.28	0.24	-0.26	108	111	20	18
185190	179.49465	-1.55768	0.020	9.01	2.45	0.32	-0.86	73	83	16	14
185252	179.54589	-1.64745	0.022	8.46	3.57	0.39	-1.7	49	48	21	18
185291	179.80472	-1.60447	0.022	8.83	2.38	0.41	-1.1	64	53	24	21
185532	180.69427	-1.59343	0.020	9.28	3.45	0.12	-0.91	88	-	17	16
185557	180.75343	-1.63802	0.019	9.62	1.13	0.24	-	113	-	23	21
185622	181.08444	-1.53028	0.005	7.87	6.13	0.29	-2.4	32	43	11	9
197419	135.20729	-0.71429	0.041	9.30	3.62	0.40	-0.58	90	103	17	14
198503	139.76575	-0.81766	0.017	8.58	0.93	0.46	-1.3	54	-	29	25
198817	140.97499	-0.68263	0.055	10.09	4.75	0.20	0.16	158	184	24	22
203148	132.84017	-0.39516	0.043	9.27	1.77	0.12	-0.26	88	-	26	25
203684	134.79005	-0.27214	0.042	9.19	3.54	0.46	-0.48	83	117	18	15
203729	135.04616	-0.30183	0.042	9.44	2.17	0.44	-0.31	99	-	53	45
203998	136.14023	-0.31481	0.028	8.93	1.60	0.09	-0.78	69	-	16	15
204096	136.52107	-0.26037	0.040	9.98	3.82	0.17	0.0099	146	158	16	15
204868	139.84670	-0.21330	0.039	9.49	1.10	0.19	-0.27	103	-	21	20
208520	129.40912	0.05067	0.035	9.65	4.74	0.16	-0.45	115	121	17	15
208892	130.75455	0.16933	0.029	9.39	7.04	0.48	-0.81	96	100	17	15
209181	132.12520	0.17087	0.058	10.30	5.53	0.23	0.79	183	173	30	27
209414	133.20974	0.15797	0.026	9.04	3.84	0.45	-1.0	75	90	24	20
209743	134.67676	0.19143	0.041	10.16	6.20	0.48	0.018	166	180	18	16
210060	136.40777	0.00327	0.019	8.98	4.92	0.21	-1.0	71	99	17	15
210567	138.74414	0.20803	0.057	9.48	5.79	0.13	-0.37	102	-	14	14
210781	139.64824	0.05988	0.055	10.22	5.31	0.24	-0.089	173	168	18	16
210808	139.75689	0.17252	0.017	8.41	1.47	0.13	-1.9	48	95	15	14
210909	140.28626	0.08058	0.024	8.44	1.73	0.49	-1.9	49	55	23	20
214245	129.52446	0.60896	0.014	9.40	1.35	0.32	-1.6	96	75	20	17
214860	131.89667	0.56184	0.058	9.75	7.03	0.49	0.003	124	104	25	21
216843	140.19242	0.60472	0.024	9.26	4.06	0.29	-0.68	87	93	21	18
220275	180.92608	1.45729	0.021	9.14	2.69	0.02	-0.89	80	-	17	17
220319	180.99245	1.48278	0.021	8.57	2.33	0.21	-1.8	53	24	16	14
220371	181.23715	1.50824	0.020	9.53	3.23	0.35	-0.93	106	134	21	18
220372	181.28939	1.55929	0.021	9.06	1.86	0.12	-1.3	76	-	18	17
220439	181.63159	1.61663	0.019	9.54	2.54	0.18	-0.26	107	134	14	13
220578	182.17817	1.45636	0.019	8.98	1.28	0.41	-0.78	71	-	17	14
220687	182.83299	1.49227	0.007	9.27	3.36	0.43	-0.75	88	74	17	15
220750	182.98977	1.48925	0.021	8.62	2.42	0.30	-0.87	55	70	16	14
221369	185.83472	1.61648	0.027	8.64	1.26	0.34	-0.56	56	-	23	20
227036	211.82817	1.28196	0.035	9.56	4.02	0.39	0.19	108	136	25	22
227223	212.67106	1.33941	0.055	10.31	4.44	0.11	0.75	185	-	31	29
227289	212.82231	1.35262	0.026	9.17	4.75	0.08	-0.68	82	-	21	20
227673	214.53595	1.22412	0.026	9.35	3.15	0.13	-0.28	93	-	24	23
227970	215.60459	1.19760	0.054	10.16	5.19	0.24	0.47	166	174	16	15
228086	216.08084	1.12442	0.039	9.18	4.21	0.20	-0.38	82	60	19	17
230174	178.74753	1.85812	0.021	8.48	1.85	0.19	-1.9	50	51	18	17
238328	213.96582	1.58638	0.025	8.82	1.36	0.36	-1.3	64	-	20	17
238395	214.24319	1.64043	0.025	9.87	2.26	0.18	0.28	135	110	31	29
238406	214.20244	1.75963	0.056	10.45	8.32	0.37	0.25	204	194	27	24
239490	217.99757	1.58140	0.030	9.21	3.68	0.19	-0.58	84	68	21	19
240108	220.62338	1.50040	0.007	9.02	1.20	0.42	-1.3	73	75	20	17
240202	221.12828	1.52201	0.005	8.66	1.29	0.21	-2.0	57	41	17	15
250277	214.43384	1.98131	0.058	10.01	5.72	0.29	0.23	149	35	31	28
251297	218.11956	1.91052	0.030	9.52	4.10	0.30	-0.31	105	116	18	16
251367	218.23409	1.89580	0.030	9.04	2.25	0.30	-0.85	75	87	21	19
252074	221.96823	1.80223	0.028	8.58	3.14	0.42	-1.3	54	30	18	15
271562	174.75468	1.33657	0.005	7.82	0.70	0.41	-0.81	31	31	24	20

GAMA ID	RA (°)	Dec (°)	$z_{\rm spec}^a$	$\log_{10}(\rm M_*)^b$ (M$_\odot$)	R_e^c (kpc)	e^d	$\log_{10}(\rm SFR)^e$ (M$_\odot$ yr^{-1})	$v_{2.2,\rm tf}^f$ (km s^{-1})	$v_{2.2}^g$ (km s^{-1})	$\sigma_{v,\rm LoS}^h$ (km s^{-1})	$\sigma_{v,z}^i$ (km s^{-1})
272996	181.66757	1.33397	0.022	8.76	1.88	0.49	-1.3	61	58	21	17
273092	181.99998	1.39593	0.037	10.07	6.27	0.25	0.19	155	37	20	18
273242	182.79525	1.44168	0.019	8.68	2.78	0.15	-1.3	58	83	19	18
273296	182.99771	1.35004	0.021	9.56	5.31	0.46	-0.28	108	68	19	16
273309	183.03839	1.31149	0.020	9.24	3.60	0.11	-1.1	86	-	19	18
273951	185.93037	1.31109	0.026	8.72	2.53	0.45	-0.38	59	7	28	24
278074	211.96000	1.13692	0.025	9.78	4.56	0.17	-1.4	126	60	15	14
278554	132.30501	0.78322	0.043	9.00	4.05	0.09	-0.68	72	-	19	18
278684	133.13103	0.85357	0.011	8.09	0.48	0.20	-1.8	38	-	24	22
278804	133.85939	0.85818	0.042	9.82	2.45	0.38	-0.97	130	-	15	13
278909	134.42490	0.81731	0.041	9.33	2.37	0.48	-0.78	92	-	15	13
279066	135.13286	0.97642	0.018	8.25	4.71	0.28	-	42	10	16	15
279818	139.43876	1.05542	0.027	9.54	4.35	0.21	-0.26	107	42	22	20
279917	139.99533	0.96084	0.018	9.32	3.88	0.44	-0.34	91	76	24	20
289107	181.04059	1.82596	0.017	9.68	3.73	0.36	-0.75	118	168	15	13
296639	212.67738	1.40807	0.046	10.22	3.13	0.18	0.17	173	132	22	20
296742	213.20535	1.48923	0.018	9.15	1.38	0.46	-1.1	81	29	31	26
296934	214.04425	1.54141	0.053	10.21	3.82	0.20	0.28	172	174	25	23
297633	216.56453	1.49149	0.055	10.43	6.88	0.25	0.38	201	175	19	17
297694	216.86676	1.33773	0.025	9.11	12.31	0.14	-1.6	78	195	15	14
298114	218.40091	1.30590	0.056	10.25	5.93	0.41	0.49	177	175	24	20
298738	221.59337	1.22840	0.050	10.06	5.64	0.43	0.15	154	154	22	19
300350	129.16480	1.13610	0.014	8.32	1.49	0.22	-3.1	45	41	18	17
300372	129.29410	1.00136	0.039	9.16	1.23	0.18	-0.86	81	-	26	24
300477	129.70677	1.12101	0.029	9.25	3.53	0.26	-0.64	87	130	22	20
300787	130.93495	1.07919	0.044	10.32	2.97	0.32	0.045	186	199	15	13
300821	131.03734	1.21435	0.013	8.82	0.98	0.29	-0.64	64	88	23	20
301346	133.52459	1.19186	0.044	10.16	3.33	0.46	0.42	166	170	28	24
301885	135.53948	1.22605	0.057	10.60	11.86	0.40	0.56	227	263	21	18
318936	212.94107	1.94731	0.018	8.90	2.77	0.36	-0.61	67	100	22	19
319150	213.62262	1.81263	0.025	8.56	1.06	0.38	-1.0	53	-	23	20
320068	216.87191	1.85175	0.029	9.17	2.38	0.28	-0.59	82	102	22	20
320281	217.63635	1.85328	0.034	9.84	3.02	0.39	-0.11	132	185	26	23
322910	129.39531	1.57389	0.031	9.74	3.61	0.19	-0.48	123	30	25	23
323194	130.81630	1.48410	0.013	8.61	0.81	0.37	-1.4	55	-	17	15
323224	130.98705	1.58429	0.013	8.61	1.02	0.11	-0.78	55	-	18	17
323242	131.00309	1.67133	0.028	9.50	1.38	0.23	-0.4	104	-	36	33
323504	131.95082	1.53447	0.063	10.94	11.71	0.09	0.41	289	-	27	26
323507	132.03504	1.56604	0.040	9.44	2.92	0.14	-0.3	99	144	23	21
323874	133.49341	1.66407	0.058	10.56	4.42	0.08	-0.61	221	-	17	17
324323	135.50044	1.78604	0.053	9.74	2.64	0.48	-0.63	123	-	12	10
325533	140.92832	2.00336	0.053	10.10	6.79	0.48	-0.12	159	172	17	15
345646	130.40960	1.96809	0.014	8.44	3.75	0.08	-1.2	49	-	25	24
346257	133.04215	1.98304	0.029	8.63	1.21	0.50	-1.1	56	-	22	19
346440	133.74686	2.13436	0.020	8.37	0.50	0.11	-1.2	46	-	19	18
346718	134.86958	2.06157	0.057	9.46	1.77	0.19	0.33	101	-	27	25
346861	135.29644	2.07820	0.055	9.82	5.15	0.33	-0.26	130	132	16	14
347263	136.99176	2.27055	0.026	9.48	2.92	0.46	-0.55	102	184	22	19
375904	131.27015	1.40141	0.014	8.07	1.06	0.35	-1.5	37	51	21	18
376165	132.17024	1.49956	0.029	8.70	2.94	0.12	-1.4	58	-	19	18
376185	132.35194	1.38501	0.034	9.07	2.16	0.30	-0.75	76	-	21	19
377348	137.33399	1.61430	0.004	7.59	0.44	0.17	-2.2	26	53	19	17
378060	140.38950	1.58462	0.017	8.70	3.10	0.34	-1.6	58	56	19	17
382152	135.42424	1.85215	0.057	10.12	6.77	0.28	-0.22	161	120	24	21
382631	137.71356	2.02189	0.055	10.09	2.92	0.16	-0.015	158	-	19	17
382764	138.26745	2.03871	0.013	9.05	1.18	0.34	-0.43	75	138	30	26
383033	139.59121	2.17020	0.027	8.47	2.22	0.31	-1.4	50	49	20	18
383259	140.67041	2.11154	0.057	10.73	6.74	0.42	0.9	249	143	39	33
383318	140.95009	2.11275	0.024	9.92	5.05	0.48	-0.085	140	66	39	33

GAMA ID	RA (°)	Dec (°)	$z_{\rm spec}^a$	$\log_{10}({\rm M}_*)^b$ (M$_\odot$)	R_e^c (kpc)	e^d	$\log_{10}({\rm SFR})^e$ (M$_\odot$ yr^{-1})	$v_{2.2,{\rm tf}}^f$ (km s^{-1})	$v_{2.2}^g$ (km s^{-1})	$\sigma_{v,{\rm LoS}}^h$ (km s^{-1})	$\sigma_{v,z}^i$ (km s^{-1})
386286	131.34372	2.19006	0.006	8.22	1.11	0.24	-1.6	42	52	20	18
386898	134.40439	2.23945	0.054	10.44	8.66	0.21	0.31	202	225	17	16
388603	140.78384	2.48607	0.017	9.80	5.50	0.12	-0.4	128	-	22	20
418624	137.09716	2.54414	0.055	10.01	4.72	0.30	-0.15	149	176	20	18
418795	137.76469	2.57229	0.039	9.13	1.62	0.24	-0.77	79	-	11	10
419632	140.75064	2.86863	0.025	8.85	1.80	0.13	-3.0	65	17	19	18
422355	130.50504	2.52837	0.028	9.26	3.18	0.04	-0.63	87	-	19	19
422359	130.55488	2.62461	0.050	10.07	2.72	0.45	0.14	155	-	14	12
422366	130.59560	2.49733	0.029	9.62	5.58	0.49	-0.35	113	90	22	18
422486	131.18034	2.57274	0.026	8.78	2.15	0.42	-0.79	62	135	21	18
422619	131.78175	2.62180	0.029	9.63	4.52	0.14	-1.8	114	97	17	16
463660	213.92314	-1.15695	0.038	9.02	3.18	0.08	-1.4	73	-	15	14
485504	216.10103	-1.76490	0.056	10.20	6.57	0.23	0.21	171	184	18	16
485529	216.24765	-1.86856	0.030	9.07	1.83	0.46	-0.36	76	-	30	25
485834	217.57879	-1.78770	0.056	10.69	6.41	0.43	0.54	242	250	29	24
485885	217.75790	-1.71721	0.055	10.25	6.09	0.16	0.76	177	167	23	21
487010	222.52592	-1.61157	0.043	9.01	2.93	0.19	-0.9	73	67	17	16
487027	222.67911	-1.71488	0.026	10.09	3.58	0.35	0.57	158	149	33	28
487175	223.33977	-1.59495	0.042	9.73	3.48	0.28	0.32	122	127	24	22
492384	216.39461	-1.37612	0.055	10.46	4.59	0.45	0.12	205	172	31	26
492414	216.50320	-1.41180	0.055	10.10	5.31	0.02	0.33	159	-	23	23
493621	221.83561	-1.30299	0.029	9.03	3.37	0.23	-1.3	74	109	20	18
493812	222.52657	-1.16131	0.043	9.54	4.59	0.45	-0.97	107	136	26	22
493825	222.43912	-1.17427	0.027	8.23	1.91	0.39	-1.3	42	51	21	18
508421	216.98916	-1.63118	0.055	10.39	4.55	0.26	-0.2	195	192	25	22
508680	217.90221	-1.59247	0.030	9.25	3.54	0.25	-0.51	87	93	16	14
509397	221.19366	-1.51910	0.056	10.24	6.82	0.19	-0.053	176	109	20	19
509444	221.32078	-1.56930	0.034	9.05	3.65	0.35	-1.2	75	88	21	18
509557	221.96775	-1.57005	0.027	8.87	0.56	0.38	-0.81	66	-	33	29
509576	221.97272	-1.37673	0.027	8.26	2.72	0.32	-0.65	43	66	20	17
509670	222.34731	-1.55925	0.027	8.95	4.31	0.43	-0.71	70	118	22	18
509852	223.13292	-1.34509	0.043	10.07	7.69	0.34	0.29	155	105	19	17
511867	216.38846	-1.11394	0.055	10.68	7.47	0.40	1.0	240	218	32	28
511921	216.67460	-1.14927	0.031	9.16	1.19	0.38	-0.46	81	-	24	21
512524	219.06927	-1.13120	0.040	9.27	5.47	0.08	-0.59	88	-	16	16
513108	221.71563	-1.14686	0.042	9.64	7.81	0.14	-0.5	114	135	25	24
514029	214.13351	-1.18215	0.050	10.49	6.38	0.30	0.51	210	187	19	17
517167	131.16137	2.41098	0.030	9.24	2.41	0.31	-0.12	86	114	19	17
517249	131.55101	2.41047	0.028	9.40	3.38	0.38	-0.29	96	83	24	21
517306	131.71344	2.56971	0.030	9.38	3.07	0.37	-0.34	95	90	22	19
517960	134.27689	2.66458	0.013	8.30	2.59	0.39	-1.4	44	28	17	15
521736	130.67894	2.87319	0.050	9.87	1.71	0.33	0.57	135	-	40	35
521768	131.07263	2.88117	0.050	10.19	4.78	0.22	0.036	169	160	22	20
521894	131.65458	2.82703	0.013	8.77	1.58	0.26	-1.5	61	106	19	17
521898	131.68612	2.79428	0.028	8.46	1.19	0.09	-1.1	49	-	22	21
534654	174.35287	-0.96382	0.050	10.31	3.84	0.03	-0.0073	185	-	22	22
534753	175.02585	-0.90142	0.029	10.35	1.14	0.33	0.22	190	-	27	24
535283	177.25575	-0.88835	0.020	8.50	0.72	0.50	-1.3	51	-	19	16
535974	179.96350	-0.85869	0.036	9.27	1.96	0.40	-0.28	88	-	21	18
537399	185.08379	-0.88202	0.040	9.63	4.51	0.32	-0.33	114	116	18	16
537476	185.39249	-1.00951	0.021	8.21	1.49	0.42	-0.56	41	23	25	22
543752	212.63639	-0.84186	0.025	8.92	5.06	0.47	-1.3	68	53	23	19
543763	212.75337	-0.90393	0.026	8.49	2.01	0.49	-1.8	50	76	20	17
543860	213.15467	-1.01222	0.054	10.01	4.94	0.20	0.31	149	44	31	28
544084	213.89591	-1.03869	0.038	9.04	5.12	0.42	-0.81	75	169	17	15
544812	216.98074	-1.00818	0.029	9.32	3.42	0.41	-1.1	91	116	17	15
544853	217.37900	-0.88385	0.035	9.54	7.30	0.18	-1.4	107	96	16	15
546043	222.74183	-0.88154	0.027	9.43	3.01	0.25	-0.36	98	104	21	19
551192	139.33882	-0.45421	0.017	8.75	0.61	0.32	-1.0	61	-	33	29

GAMA ID	RA (°)	Dec (°)	$z_{\rm spec}^a$	$\log_{10}({\rm M}_*)^b$ (M$_\odot$)	R_e^c (kpc)	e^d	$\log_{10}({\rm SFR})^e$ (M$_\odot$ yr^{-1})	$v_{2.2,{\rm tf}}^f$ (km s^{-1})	$v_{2.2}^g$ (km s^{-1})	$\sigma_{v,{\rm LoS}}^h$ (km s^{-1})	$\sigma_{v,z}^i$ (km s^{-1})
551368	140.01779	-0.50248	0.026	8.88	1.09	0.04	-1.2	66	-	24	23
558887	174.37404	-0.47340	0.029	8.83	2.28	0.40	-0.97	64	77	21	18
559292	176.41768	-0.57082	0.028	8.71	2.52	0.47	-0.58	59	41	26	22
559300	176.53218	-0.45799	0.013	8.64	1.23	0.23	-1.7	56	46	18	16
559495	177.34230	-0.62371	0.040	9.05	3.20	0.43	-0.18	75	138	21	18
560333	179.98443	-0.54822	0.022	9.90	5.52	0.18	-0.18	138	154	17	16
560718	181.33290	-0.48020	0.005	7.76	0.50	0.14	-3.0	30	63	18	17
560946	182.33179	-0.52747	0.035	9.19	3.44	0.35	-0.97	83	88	13	12
561143	183.01351	-0.60685	0.035	9.54	4.33	0.47	0.15	107	64	37	31
567676	212.76660	-0.54511	0.026	8.57	2.42	0.17	-1.8	53	21	23	21
567736	213.05273	-0.61270	0.025	8.69	1.81	0.47	0.32	58	15	28	23
567760	213.07541	-0.56930	0.025	8.46	4.69	0.28	-0.47	49	57	11	10
570119	222.13518	-0.57531	0.043	9.56	5.51	0.48	0.43	108	134	24	20
570174	222.60503	-0.46932	0.042	9.81	9.83	0.29	-0.76	129	104	23	20
573586	129.12557	-0.08624	0.052	10.03	4.42	0.24	0.027	151	148	25	22
574008	131.02735	-0.10350	0.051	10.18	6.14	0.47	0.56	168	144	28	24
574029	131.07729	-0.04921	0.051	10.04	3.17	0.23	0.56	152	-	27	24
574193	134.43437	-0.04481	0.044	8.73	5.02	0.18	-0.63	60	123	19	17
574572	136.33633	-0.03700	0.019	8.76	0.79	0.08	-1.6	61	-	17	17
574617	136.43827	-0.19325	0.076	10.33	4.12	0.15	0.46	187	-	24	22
574692	136.73747	-0.12355	0.019	9.31	1.82	0.37	-0.41	90	36	23	20
583443	174.88168	-0.15990	0.028	8.93	1.99	0.15	-0.92	69	97	22	20
583637	175.82494	-0.18161	0.056	10.01	4.10	0.05	0.11	149	-	23	22
584013	177.87898	-0.07776	0.048	10.46	3.79	0.29	0.75	205	85	34	30
585121	181.19288	-0.01538	0.040	9.55	2.68	0.27	-0.42	107	139	31	28
585231	181.78147	-0.02019	0.021	8.76	2.15	0.41	-1.6	61	72	17	15
592863	214.33856	-0.16910	0.044	9.46	6.05	0.14	-0.37	101	98	20	19
592999	215.06156	-0.07938	0.053	10.26	4.92	0.47	0.3	178	197	27	23
593526	216.81878	-0.09008	0.031	9.32	1.64	0.49	-0.55	91	-	24	20
594059	218.90933	-0.09702	0.029	9.48	4.95	0.31	-0.87	102	96	21	19
594906	222.36208	-0.16420	0.041	9.77	1.66	0.31	0.22	126	-	26	23
594990	222.80149	-0.06085	0.044	10.34	3.72	0.26	-2.1	189	191	30	27
598911	129.30130	0.38743	0.042	9.39	6.87	0.21	-0.27	96	81	19	17
598968	129.56040	0.35208	0.042	10.06	6.74	0.20	0.12	154	121	19	18
599095	130.13599	0.26201	0.035	9.44	2.72	0.34	-1.0	99	115	23	20
599134	130.26050	0.39590	0.037	9.09	2.21	0.38	-0.63	77	-	25	22
599329	131.10371	0.34289	0.015	8.40	0.71	0.33	-1.1	47	-	29	25
599862	132.74012	0.23892	0.041	9.04	4.62	0.14	-0.83	75	123	12	11
600026	133.48520	0.21557	0.051	10.28	5.00	0.28	0.46	181	203	30	26
600312	134.81541	0.39164	0.011	8.86	0.76	0.25	-0.97	66	55	27	24
601323	139.34146	0.32191	0.054	10.73	8.32	0.31	0.32	249	130	30	27
601395	139.56851	0.38503	0.017	8.91	8.81	0.26	-1.4	68	2	29	26
610474	180.39356	0.34748	0.039	10.01	2.40	0.24	0.45	149	-	30	27
610997	182.86904	0.37865	0.020	9.32	2.55	0.22	-0.83	91	118	25	23
611629	185.50338	0.31504	0.034	9.46	1.38	0.33	-0.5	101	-	26	23
617655	212.63506	0.22418	0.029	9.07	3.24	0.14	-2.4	76	104	17	16
617945	213.72345	0.40730	0.028	8.47	0.91	0.22	-1.0	50	-	21	19
618071	214.01854	0.21626	0.026	8.94	5.14	0.37	-0.8	69	62	21	18
618116	214.40555	0.32910	0.051	10.25	6.47	0.27	0.37	177	179	27	24
618152	214.52287	0.22739	0.053	10.01	4.18	0.29	-0.15	149	32	23	20
619095	218.03502	0.41114	0.053	10.47	3.69	0.32	0.6	207	211	31	27
622333	132.56179	0.75988	0.043	9.03	3.61	0.24	-	74	42	18	17
622394	133.06978	0.68110	0.041	9.22	3.17	0.28	-0.57	85	173	24	22
622744	134.82995	0.79776	0.013	9.16	1.58	0.46	-0.43	81	65	28	24
622770	134.98662	0.78816	0.052	10.01	2.36	0.48	-0.4	149	-	34	29
623366	138.54711	0.81821	0.055	10.42	6.71	0.06	0.26	200	-	20	19
623712	140.13867	0.72106	0.017	9.16	2.83	0.08	-1.4	81	-	19	18

This paper has been typeset from a TeX/LaTeX file prepared by the author.